Multiplets at zero magnetic field: The geometry of zero-field NMR

Mark C. Butler, Micah P. Ledbetter, Thomas Theis, John W. Blanchard, Dmitry Budker et al.

Citation: J. Chem. Phys. **138**, 184202 (2013); doi: 10.1063/1.4803144
View online: http://dx.doi.org/10.1063/1.4803144
View Table of Contents: http://jcp.aip.org/resource/1/JCPSA6/v138/i18
Published by the American Institute of Physics.

Multiplets at zero magnetic field: The geometry of zero-field NMR

Mark C. Butler,[1,2,a)] Micah P. Ledbetter,[3] Thomas Theis,[1,2,b)] John W. Blanchard,[1,2] Dmitry Budker,[3,4] and Alexander Pines[1,2]
[1]*Materials Sciences Division, Lawrence Berkeley National Laboratory, Berkeley, California 94720, USA*
[2]*Department of Chemistry, University of California, Berkeley, California 94720, USA*
[3]*Department of Physics, University of California, Berkeley, California 94720, USA*
[4]*Nuclear Science Division, Lawrence Berkeley National Laboratory, Berkeley, California 94720, USA*

(Received 6 February 2013; accepted 15 April 2013; published online 10 May 2013)

For liquid samples at Earth's field or below, nuclear-spin motion within scalar-coupled networks yields multiplets as a spectroscopic signature. In weak fields, the structure of the multiplets depends on the magnitude of the Zeeman interaction relative to the scalar couplings; in Earth's field, for example, heteronuclear couplings are truncated by fast precession at distinct Larmor frequencies. At zero field, weak scalar couplings are truncated by the relatively fast evolution associated with strong scalar couplings, and the truncated interactions can be described geometrically. When the spin system contains a strongly coupled subsystem A, an average over the fast evolution occurring within the subsystem projects each strongly coupled spin onto $\mathbf{F}_A$, the summed angular momentum of the spins in A. Weakly coupled spins effectively interact with $\mathbf{F}_A$, and the coupling constants for the truncated interactions are found by evaluating projections. We provide a formal description of zero-field spin systems with truncated scalar couplings while also emphasizing visualization based on a geometric model. The theoretical results are in good agreement with experimental spectra that exhibit second-order shifts and splittings. © *2013 AIP Publishing LLC*. [http://dx.doi.org/10.1063/1.4803144]

I. INTRODUCTION

Experiments involving nuclear magnetic resonance (NMR) are typically performed in strong magnetic fields, which are advantageous for polarization of the spins and for sensitive inductive detection.[1] A strong field is also needed to resolve chemical shifts; for example, protein-structure determination[2] by means of NMR requires the presence of a large static field that maximizes the frequency spacing between peaks corresponding to different amino-acid residues.

In recent years, however, there has been a growing interest in nuclear magnetic resonance in Earth's field[3–8] (∼50 μT), as well as in microtesla and submicrotesla fields,[9–14] and in the zero-field regime,[15–21] where the Zeeman interaction with external fields is negligible compared to the couplings between nuclei. Samples can be prepolarized by thermal equilibration in a relatively large field before detection in a weaker field[22] or at zero field,[18] or they can be hyperpolarized, for example, by dynamic nuclear polarization,[23,24] parahydrogen-induced polarization,[16,17,25,26] or spin-exchange optical pumping.[27] At low frequencies where the sensitivity of inductive detection is poor, a superconducting quantum interference device[14,28] or an atomic magnetometer[29–31] can be used for signal acquisition.

Motivations for performing experiments without a strong applied field include the availability of portable, low-cost instrumentation for low-field inductive detection;[3,5,6] the potential for portable, cryogen-free instrumentation for optical detection;[29,30,32] the ease with which high absolute field homogeneity and narrow lines can be obtained,[6,14] particularly at zero field;[15,17,18] enhanced contrast in relaxation times;[33–35] minimal magnetic-susceptibility artifacts, decreased screening by eddy currents in conductive samples;[33,36–38] and the capability for convenient *in situ* measurements, for example, in geophysical applications[39,40] and in the detection of explosives.[33]

Chemical shifts are of central importance for high-field NMR spectroscopy, and the absence of resolvable chemical shifts (except in unusual cases[27]) is an important distinguishing feature of spectroscopic measurements at Earth's field or below. In weak fields and at zero field, scalar-coupled networks yield multiplets as a spectroscopic signature. Multiplets associated with heteronuclear couplings have been detected with high resolution in weak fields,[6,14] and two-dimensional correlation spectroscopy has been demonstrated in Earth's field,[41] with transfer of coherence yielding cross peaks at the Larmor frequencies of ^{1}H and ^{19}F. Homonuclear couplings can also be measured in weak fields, provided heteronuclear couplings break the magnetic equivalence of the protons.[42] Decreasing the field from tens of microtesla to zero moves an isotropic liquid sample from a regime where the Zeeman interaction is dominant to a regime where coherent spin evolution is governed only by the scalar-coupling Hamiltonian H_J. For a set of equivalent protons coupled to a single heteronucleus of spin 1/2, the dependence of the spectrum on field strength has been characterized, and boundaries that mark changes in complexity have been identified.[43] Perturbation theory has been used to analyze multiplets of strongly coupled heteronuclear systems in Earth's field,[44] where the

a)Electronic mail: mrkcbutler@gmail.com. Present address: William R. Wiley Environmental Molecular Sciences Laboratory, Pacific Northwest National Laboratory, Richland, Washington 99352, USA.
b)Present address: Department of Chemistry, Duke University, Durham, North Carolina 27708, USA.

scalar coupling is the perturbation, and in the near-zero-field regime,[9] where the Zeeman interaction is the perturbation. Multiplets are also observed at zero field, due to the presence of weak scalar couplings that split the energy degeneracy associated with the strong couplings in H_J.[15,18,45]

Here we describe the truncation of weak scalar couplings in a zero-field environment due to the fast evolution associated with strong scalar couplings, and we use perturbation theory to characterize the resulting multiplets in simple systems. We assume that residual magnetic fields can be neglected, as in previously reported experiments where magnetic shields and coils decreased the field to ∼0.1nT.[15–18] Taking account of the spherical symmetry of the problem leads to a geometric description of the truncated interactions. When the spin system contains a strongly coupled subsystem A, an average over the fast evolution occurring within the subsystem projects each strongly coupled spin onto $\mathbf{F}_A$, the summed angular momentum of the spins in A. Weakly coupled spins effectively interact with $\mathbf{F}_A$, and the coupling constants for the truncated interactions are found by evaluating projections. Section II presents a geometric model of the spin motion in a system consisting of a heteronucleus S and two protons I_A and I_B, where S and I_A constitute the strongly coupled subsystem. The model is formalized in Sec. III by means of the projection theorem, and in Sec. IV, the formal description is extended to systems consisting of a heteronucleus S and two sets of equivalent protons, with one set of protons strongly coupled to S. We follow the nomenclature of Refs. 15 and 45 in letting $(XA_n)B_m$ denote this class of spin systems, where X represents the heteronucleus, A_n represents a set of n equivalent protons strongly coupled to X, and B_m represents a set of m equivalent protons weakly coupled to X and A_n. The importance of second-order effects in the multiplets of $(XA_n)B_m$ systems is illustrated by experimental spectra presented in Secs. III and IV. In Sec. V, the geometric description of truncated weak interactions is generalized to systems that can be divided into strongly coupled and weakly coupled subsystems.

II. GEOMETRIC MODEL

The vector model of the atom[46,47] describes the motion of coupled angular momenta as the precession of classical vectors. This model can be adapted to yield a geometric description of the truncation of weak scalar couplings at zero field, and the geometric description can be formalized using the projection theorem. We consider a three-spin system containing a heteronucleus $S = 1/2$ and protons I_A and I_B, with I_A strongly coupled to S, and I_B weakly coupled to the other two spins. The summed angular momentum of the strongly coupled spins is denoted by

$$\mathbf{F}_A = \mathbf{S} + \mathbf{I}_A.$$

In the absence of any coupling to spin I_B, the two strongly coupled spins can be visualized as vectors that precess about $\mathbf{F}_A$, which is motionless. This motion is depicted in Fig. 1(a).

When $\mathbf{I}_B$ is weakly coupled to $\mathbf{S}$ and $\mathbf{I}_A$, the weak interactions are averaged over the fast precession about $\mathbf{F}_A$, so that $\mathbf{I}_B$ effectively interacts with the projections of $\mathbf{S}$ and $\mathbf{I}_A$ onto $\mathbf{F}_A$, as illustrated in Fig. 1(b). We denote these projections by $\mathbf{S}^{\|}$ and $\mathbf{I}_A^{\|}$, respectively. Since the projections are proportional to $\mathbf{F}_A$, the truncated weak interaction couples $\mathbf{I}_B$ to $\mathbf{F}_A$. Figure 1(c) depicts the motion associated with the truncated interaction, which causes $\mathbf{I}_B$ and $\mathbf{F}_A$ to precess about the motionless vector

$$\mathbf{F} = \mathbf{F}_A + \mathbf{I}_B.$$

Figure 1(d) shows that the slow precession of $\mathbf{F}_A$ modulates the fast motion of the strongly coupled spins. The modulated motion is described by a pair of closely spaced high-frequency Fourier components, which yields a doublet in the spectrum. The motion of $\mathbf{I}_B$ and $\mathbf{F}_A$ yields a single low-frequency peak. (Note that we use "high-frequency" and "low-frequency" to refer to regions of the spectrum where the strong and weak scalar couplings, respectively, are characteristic transition frequencies.)

This geometric model can be used to find the coupling constant associated with the truncated interaction. The scalar-coupling Hamiltonian is

$$H_J = H_0 + H_1, \tag{1}$$

where

$$H_0 = J_{SA}\,\mathbf{S}\cdot\mathbf{I}_A \tag{2}$$

is the strong coupling and

$$H_1 = J_{SB}\,\mathbf{S}\cdot\mathbf{I}_B + J_{AB}\,\mathbf{I}_A\cdot\mathbf{I}_B \tag{3}$$

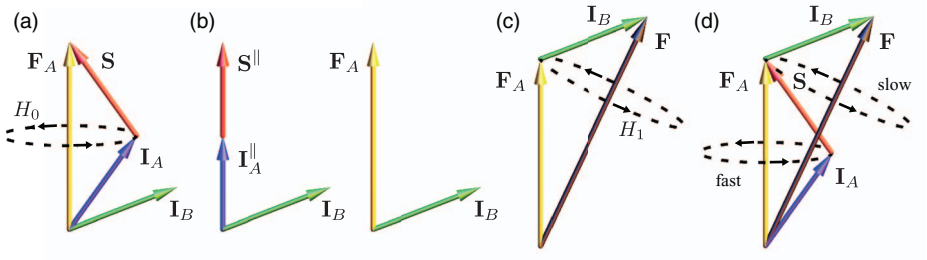

FIG. 1. Vector model of the spin motion in a system containing a heteronucleus $\mathbf{S}$ and two protons $\mathbf{I}_A$ and $\mathbf{I}_B$, with $\mathbf{I}_A$ strongly coupled to $\mathbf{S}$, and $\mathbf{I}_B$ weakly coupled to the other two spins. The strong coupling and the weak couplings are represented by the Hamiltonians H_0 and H_1, respectively. (a) If the weak couplings involving spin $\mathbf{I}_B$ are negligible, the strongly coupled spins $\mathbf{S}$ and $\mathbf{I}_A$ precess about a motionless vector that represents $\mathbf{F}_A$, the sum of their angular momenta. (b) Weak scalar couplings involving spin $\mathbf{I}_B$ are averaged over this fast precession, so that $\mathbf{I}_B$ "sees" the projections $\mathbf{S}^{\|}$ and $\mathbf{I}_A^{\|}$ rather than the instantaneous states of $\mathbf{S}$ and $\mathbf{I}_A$. The truncated weak interaction therefore couples $\mathbf{I}_B$ to $\mathbf{F}_A$. (c) The truncated interaction causes $\mathbf{I}_B$ and $\mathbf{F}_A$ to precess about the total angular momentum $\mathbf{F}$. (d) The slow precession of $\mathbf{F}_A$ modulates the fast motion of $\mathbf{S}$ and $\mathbf{I}_A$, which yields a high-frequency doublet in the spectrum. The precession of $\mathbf{I}_B$ and $\mathbf{F}_A$ about $\mathbf{F}$ is also detectable as a single low-frequency peak.

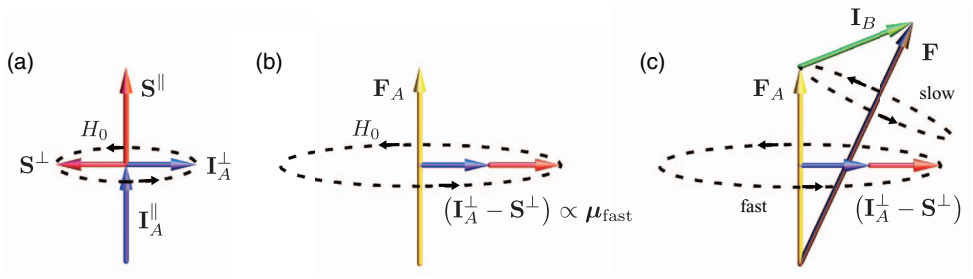

FIG. 2. Spin vectors associated with the fast dipole oscillations. (a) Under H_0, the strongly coupled spins precess about $\mathbf{F}_A$. The components $\mathbf{S}^{\parallel}$ and $\mathbf{I}_A^{\parallel}$ are proportional to $\mathbf{F}_A$ and thus do not evolve. The precession involves motion of $\mathbf{I}_A^{\perp}$ and $\mathbf{S}^{\perp}$, the components of $\mathbf{I}_A$ and $\mathbf{S}$ that are perpendicular to $\mathbf{F}_A$. (b) Since the gyromagnetic ratios for $\mathbf{I}$ and $\mathbf{S}$ are different, the spin vector $(\mathbf{I}_A^{\perp} - \mathbf{S}^{\perp})$ has a dipole moment $\boldsymbol{\mu}_{\text{fast}}$ that precesses quickly under H_0. (c) This motion is modulated by the slow precession of $\mathbf{F}_A$ under the truncated weak coupling. The modulated motion of $\boldsymbol{\mu}_{\text{fast}}$ is responsible for the high-frequency peaks in the spectrum.

is the perturbation. In Eqs. (2) and (3), J_{SA}, J_{SB}, and J_{AB} are coupling constants that are conventionally expressed in Hz. (Consistent with this convention, energies are expressed in Hz throughout this paper.) Averaging over the fast evolution associated with H_0 replaces $\mathbf{S}$ and $\mathbf{I}_A$ in Eq. (3) by $\mathbf{S}^{\parallel}$ and $\mathbf{I}_A^{\parallel}$, respectively. The perturbation can therefore be approximated as

$$H_1^{(1)} = J_{SB}\,\mathbf{S}^{\parallel} \cdot \mathbf{I}_B + J_{AB}\,\mathbf{I}_A^{\parallel} \cdot \mathbf{I}_B, \tag{4}$$

where the notation $H_1^{(1)}$ is chosen to reflect the fact that in a formal analysis, the replacement of H_1 by $H_1^{(1)}$ corresponds to the use of a first-order effective Hamiltonian. Since the vectors $\mathbf{S}$ and $\mathbf{I}_A$ have the same length,

$$\mathbf{S}^{\parallel} = \mathbf{I}_A^{\parallel} = \frac{1}{2}\mathbf{F}_A, \tag{5}$$

as illustrated in Fig. 1(b). We can thus rewrite Eq. (4) as

$$H_1^{(1)} = \left(\frac{J_{SB} + J_{AB}}{2}\right)\mathbf{F}_A \cdot \mathbf{I}_B. \tag{6}$$

From Eq. (6), the coupling constant for the truncated interaction is $(J_{SB} + J_{AB})/2$. The factor of 2 in the denominator can be interpreted as scaling of the coupling constants J_{SB} and J_{AB} by the projection of $\mathbf{S}$ and $\mathbf{I}_A$ onto $\mathbf{F}_A$.

The observable in our experiments is the spin magnetic dipole, given by

$$\boldsymbol{\mu} = \gamma_S\hbar\mathbf{S} + \gamma_I\hbar\mathbf{I}_A + \gamma_I\hbar\mathbf{I}_B, \tag{7}$$

where γ_S and γ_I are the gyromagnetic ratio of the heteronucleus and the ^{1}H nucleus, respectively. In describing the high-frequency dipole oscillations associated with the motion of $\mathbf{S}$ and $\mathbf{I}_A$, we write the first two terms on the right side of Eq. (7) as[20]

$$\gamma_S\hbar\mathbf{S} + \gamma_I\hbar\mathbf{I}_A = \frac{\gamma_I + \gamma_S}{2}\hbar\mathbf{F}_A + \frac{\gamma_I - \gamma_S}{2}\hbar(\mathbf{I}_A - \mathbf{S}). \tag{8}$$

In the absence of the perturbation H_1, the vector $\mathbf{F}_A$ is constant, and the motion of $(\mathbf{I}_A - \mathbf{S})$ governed by H_0 causes $\boldsymbol{\mu}$ to evolve. The proportionality constant $(\gamma_I - \gamma_S)/2$ is roughly analogous to a gyromagnetic ratio, since it characterizes the strength of the dipole moment associated with $(\mathbf{I}_A - \mathbf{S})$. Within the geometric model, the motion of $(\mathbf{I}_A - \mathbf{S})$ can be visualized as the precession of components $\mathbf{I}_A^{\perp}$, $\mathbf{S}^{\perp}$ that are perpendicular to $\mathbf{F}_A$, as shown in Figs. 2(a) and 2(b). In Fig. 2(c), modulation of this motion by the perturbation is depicted.

To describe the dipole oscillations associated with the low-frequency motion of $\mathbf{I}_B$ and $\mathbf{F}_A$, we express $\boldsymbol{\mu}$ in the form

$$\boldsymbol{\mu} = \frac{\gamma_I + \gamma_S}{2}\hbar\mathbf{F}_A + \frac{\gamma_I - \gamma_S}{2}\hbar(\mathbf{I}_A - \mathbf{S}) + \gamma_I\hbar\mathbf{I}_B$$

and drop the term proportional to $(\mathbf{I}_A - \mathbf{S})$, which is responsible for the high-frequency oscillations. Writing the remaining two terms as

$$\frac{\gamma_I + \gamma_S}{2}\hbar\mathbf{F}_A + \gamma_I\hbar\mathbf{I}_B = \frac{3\gamma_I + \gamma_S}{4}\hbar\mathbf{F} + \frac{\gamma_I - \gamma_S}{4}\hbar(\mathbf{I}_B - \mathbf{F}_A), \tag{9}$$

we note that the vector $\mathbf{F}$ is constant, while $(\gamma_I - \gamma_S)/4$ characterizes the strength of the low-frequency dipole oscillations associated with the motion of $(\mathbf{I}_B - \mathbf{F}_A)$. Comparison of Eqs. (8) and (9) shows that the "effective gyromagnetic ratio" for $(\mathbf{I}_B - \mathbf{F}_A)$ is smaller by a factor of two than for $(\mathbf{I}_A - \mathbf{S})$. As illustrated in Fig. 3, the motion of $(\mathbf{I}_B - \mathbf{F}_A)$ can be visualized as the precession of components $\mathbf{I}_B^{\perp}$, $\mathbf{F}_A^{\perp}$ that are perpendicular to $\mathbf{F}$.

We conclude this section by briefly reviewing the limitations of the vector model, which are discussed in greater detail in Ref. 46. Note first that when the spin system is in a stationary state, the expectation values of spin operators do not vary with time. A correspondence between quantum-mechanical expectation values and the vectors shown in Figs. 1–3 can thus only exist when a coherence is present. Certain forms of coherence yield evolution that closely matches the predictions of the vector model, but the evolution can also take forms not predicted by the model. For example, the experimental protocol described in Sec. III C yields dipole oscillations along the z axis only, with $\langle\mu_x(t)\rangle = \langle\mu_y(t)\rangle = 0$.

III. FORMAL GEOMETRIC DESCRIPTION OF A THREE-SPIN SYSTEM

In Secs. III–V, we show that for a broad range of scalar-coupled networks, equations obtained from the geometric model can be derived formally, which justifies the use of the model for gaining intuition about zero-field NMR experiments. In the derivations, the projection theorem[48] is used to find the restriction of spin operators to a single angular-momentum manifold. In order to make the discussion as

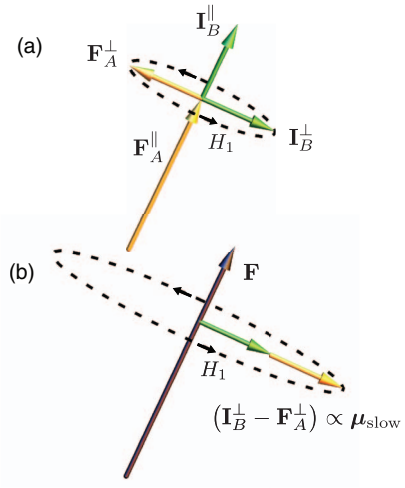

FIG. 3. Spin vectors associated with the slow dipole oscillations. (a) Under the truncated weak coupling, $\mathbf{I}_B$ and $\mathbf{F}_A$ precess about the total angular momentum $\mathbf{F}$. The precession involves motion of $\mathbf{I}_B^{\perp}$ and $\mathbf{F}_A^{\perp}$, the components of $\mathbf{I}_B$ and $\mathbf{F}_A$ that are perpendicular to $\mathbf{F}$. (b) The dipole moment $\boldsymbol{\mu}$ includes contributions $\gamma_I \hbar \mathbf{I}_B$ and $(\gamma_I + \gamma_S)\hbar/2\,\mathbf{F}_A$. Because γ_I is different than the effective gyromagnetic ratio associated with $\mathbf{F}_A$, the spin vector $(\mathbf{I}_B^{\perp} - \mathbf{F}_A^{\perp})$ has a dipole moment $\boldsymbol{\mu}_{\text{slow}}$ that precesses under H_1 and contributes a low-frequency peak.

self-contained as possible, we include in Sec. III A a review of the projection theorem and simple methods for evaluating projections. This review is given in the context of a formal description of the same three-spin system modeled geometrically in Sec. II. The system contains a heteronucleus $S = 1/2$ and two protons I_A and I_B, with I_A strongly coupled to S, and I_B weakly coupled to the other two spins. The Hamiltonian is given by Eqs. (1)–(3). In Sec. III A, we obtain an expression for the truncated weak Hamiltonian and second-order estimates of the energies. Section III B shows that the high-frequency and low-frequency spectra of $\langle \boldsymbol{\mu}(t) \rangle$ are associated with the motion of operators $(\mathbf{I}_A^{\perp} - \mathbf{S}^{\perp})$ and $(\mathbf{I}_B^{\perp} - \mathbf{F}_A^{\perp})$, respectively, whose definitions are motivated by the geometric model. Section III C discusses the amplitudes and phases of the peaks in the zero-field spectrum and presents example spectra.

Note that the approach used here to describe nuclear-spin systems is closely related to well-known methods for analyzing the fine and hyperfine structure of atoms. For example, the Landé g-factor for atomic energy levels is commonly evaluated by using the projection theorem to find the restriction of spin operators to single angular-momentum manifolds.[48]

A. Energy levels

We use perturbation theory to find zero-order eigenstates and second-order energies for the three-spin system, where H_1 of Eq. (3) is treated as the perturbation. The unperturbed Hamiltonian H_0 acts only on spins I_A and S, and its eigenstates can be written in the form $|\phi\rangle|\psi\rangle$, where $|\phi\rangle$ is a state of the two strongly coupled spins and $|\psi\rangle$ is an arbitrary state of spin I_B. Because of the spherical symmetry of the scalar-coupling Hamiltonian with respect to spin rotations, the two-spin eigenstates $|\phi\rangle$ can be grouped into degenerate angular-momentum manifolds labeled with quantum number F_A, the summed angular momentum of the strongly coupled spins. In particular, the unperturbed eigenstates of H_0 can be written as $|F_A, m_A\rangle|\psi\rangle$, where F_A is 0 or 1, and where m_A is the z component of the angular momentum F_A. States with $F_A = 0$ have energy $-3J_{SA}/4$ under H_0, while states with $F_A = 1$ have energy $J_{SA}/4$.[18]

To find zero-order eigenstates and first-order energies of H_J, we diagonalize the perturbation H_1 within the degenerate eigenspaces of H_0. In describing the couplings introduced by H_1 within these degenerate spaces, we first consider the matrix elements of the operator $\mathbf{S} \cdot \mathbf{I}_B$ that appears on the right side of Eq. (3). For a pair of states $|F_A, m_A\rangle|\psi\rangle$ and $|F_A, m'_A\rangle|\psi'\rangle$ that are degenerate under H_0, we obtain the matrix element

$$\langle\psi|\langle F_A, m_A|\,\mathbf{S}\cdot\mathbf{I}_B\,|F_A, m'_A\rangle|\psi'\rangle = \langle F_A, m_A|\mathbf{S}|F_A, m'_A\rangle \cdot \langle\psi|\mathbf{I}_B|\psi'\rangle. \tag{10}$$

Because $\mathbf{S}$ is a vector operator, the Wigner-Eckart theorem implies that

$$\langle F_A, m_A|\mathbf{S}|F_A, m'_A\rangle \propto \langle F_A, m_A|\mathbf{F}_A|F_A, m'_A\rangle, \tag{11}$$

and the proportionality constant does not depend on m_A or m'_A. The projection theorem[48] expresses this proportionality constant in the form

$$\frac{\langle F_A, m_A|\mathbf{S}\cdot\mathbf{F}_A|F_A, m_A\rangle}{\langle F_A, m_A|\mathbf{F}_A\cdot\mathbf{F}_A|F_A, m_A\rangle} = \frac{\langle \mathbf{S}\cdot\mathbf{F}_A\rangle}{\langle \mathbf{F}_A\cdot\mathbf{F}_A\rangle}, \tag{12}$$

where the expectation values $\langle \mathbf{S}\cdot\mathbf{F}_A\rangle$, $\langle \mathbf{F}_A\cdot\mathbf{F}_A\rangle$ do not depend on m_A. Using (11) and (12), we define

$$\mathbf{S}^{\parallel} = \frac{\langle \mathbf{S}\cdot\mathbf{F}_A\rangle}{\langle \mathbf{F}_A\cdot\mathbf{F}_A\rangle}\mathbf{F}_A \tag{13}$$

as the projection of $\mathbf{S}$ onto $\mathbf{F}_A$. The matrix element of Eq. (10) can then be written as

$$\langle F_A, m_A|\mathbf{S}^{\parallel}|F_A, m'_A\rangle \cdot \langle\psi|\mathbf{I}_B|\psi'\rangle.$$

For the purpose of diagonalizing the perturbation within a degenerate subspace of H_0, we can replace the operator $\mathbf{S}\cdot\mathbf{I}_B$ by $\mathbf{S}^{\parallel}\cdot\mathbf{I}_B$ in Eq. (3). Similar arguments show that $\mathbf{I}_A\cdot\mathbf{I}_B$ can be replaced by $\mathbf{I}_A^{\parallel}\cdot\mathbf{I}_B$, where

$$\mathbf{I}_A^{\parallel} = \frac{\langle \mathbf{I}_A\cdot\mathbf{F}_A\rangle}{\langle \mathbf{F}_A\cdot\mathbf{F}_A\rangle}\mathbf{F}_A. \tag{14}$$

Making these replacements in Eq. (3), we recover Eq. (4) as the first-order description of the perturbation, where the projections $\mathbf{S}^{\parallel}$ and $\mathbf{I}_A^{\parallel}$ depend on F_A. Note that Eqs. (13) and (14) can be interpreted geometrically, since projection of classical vectors would give expressions of the same form.

To evaluate $\mathbf{S}^{\parallel}$, we use a standard algebraic trick. From

$$\mathbf{I}_A^2 = (\mathbf{F}_A - \mathbf{S})^2 = \mathbf{F}_A^2 + \mathbf{S}^2 - 2\mathbf{S}\cdot\mathbf{F}_A,$$

we obtain

$$\mathbf{S}\cdot\mathbf{F}_A = \frac{1}{2}\left(\mathbf{F}_A^2 + \mathbf{S}^2 - \mathbf{I}_A^2\right),$$

which gives

$$\langle \mathbf{S}\cdot\mathbf{F}_A\rangle = \frac{1}{2}[F_A(F_A+1)+S(S+1) - I_A(I_A+1)] \quad (15)$$

and

$$\mathbf{S}^{\parallel} = \frac{F_A(F_A+1)+S(S+1)-I_A(I_A+1)}{2F_A(F_A+1)}\mathbf{F}_A. \quad (16)$$

Similar manipulations yield

$$\mathbf{I}_A^{\parallel} = \frac{F_A(F_A+1)+I_A(I_A+1)-S(S+1)}{2F_A(F_A+1)}\mathbf{F}_A. \quad (17)$$

Evaluating Eqs. (16) and (17) for the manifold with $F_A = 1$, we recover Eq. (5) of the geometric model. Within this manifold, the first-order approximation to H_1 is therefore given by Eq. (6) as

$$H_1^{(1)} = \left(\frac{J_{SB}+J_{AB}}{2}\right)\mathbf{F}_A\cdot\mathbf{I}_B.$$

For the manifold with $F_A = 0$, the projections of $\mathbf{S}$ and $\mathbf{I}_A$ onto $\mathbf{F}_A$ are zero, which gives $H_1^{(1)} = 0$. Equations (5) and (6) can be considered to hold trivially in this case as well.

To find the zero-order eigenstates of H_J, we recall that the degenerate eigenspaces of H_0 each consist of a set of product states $|F_A, m_A\rangle|\psi\rangle$ that have the same value of F_A. We can visualize each of these spaces as the product space of two spins F_A and I_B that interact through a scalar coupling $\mathbf{F}_A\cdot\mathbf{I}_B$. Because the coupling is invariant under a uniform rotation of the two spins, the resulting eigenstates can be grouped into degenerate manifolds of the total angular momentum F. Explicit formulas for the eigenstates can be found by using the Clebsch-Gordan coefficients to add the angular momenta F_A and I_B. Since

$$\mathbf{F}_A\cdot\mathbf{I}_B = \frac{1}{2}\left(\mathbf{F}^2-\mathbf{F}_A^2-\mathbf{I}_B^2\right),$$

the first-order energy correction is

$$\Delta^{(1)} = \frac{1}{4}(J_{SB}+J_{AB}) \times [F(F+1)-F_A(F_A+1)-I_B(I_B+1)]. \quad (18)$$

We outline the derivation of the second-order energy corrections $\Delta^{(2)}$, which is presented in greater detail in the Appendix. The second-order corrections can be calculated using nondegenerate perturbation theory, because the matrix elements of H_1 that were neglected in the first-order estimates of the energies introduce couplings only within isolated subspaces spanned by states with distinct zero-order energies. To evaluate the matrix elements of H_1 within these subspaces, we use the Wigner 6j symbols to express the zero-order eigenstates in basis sets where the operators $\mathbf{S}\cdot\mathbf{I}_B$ and $\mathbf{I}_A\cdot\mathbf{I}_B$ are diagonal. Algebraic manipulations similar to those performed in deriving Eqs. (15) and (18) yield analytic expressions for the eigenvalues of these operators, which in turn yield analytic expressions for the matrix elements of H_1 that couple states with distinct zero-order energies. Substitution of these expressions into the standard formulas of nondegenerate perturbation theory and simplification of the resulting equations yields the second-order energy corrections shown in Table I.

TABLE I. Approximate energy levels of the three-spin system. The zero-order eigenstates can be grouped into degenerate angular-momentum manifolds labeled with quantum numbers S, I_A, F_A, I_B, and F. All of the manifolds have $S = I_A = I_B = 1/2$; the values of F_A and F are shown in the table. The zero-order energy is denoted by $E^{(0)}$, while the first-order and second-order energy corrections are denoted by $\Delta^{(1)}$ and $\Delta^{(2)}$, respectively. The energy level with $F_A = 0$ has $\Delta^{(1)} = 0$ because the projections of $\mathbf{S}$ and $\mathbf{I}_A$ onto $\mathbf{F}_A$ are zero within this level. Because H_1 is a scalar operator, it does not couple states that have distinct values of F. As a result, $\Delta^{(2)} = 0$ for the energy level with $F = 3/2$, which is not coupled to the two levels with $F = 1/2$.

Angular momenta	$E^{(0)}$	$\Delta^{(1)}$	$\Delta^{(2)}$
$F_A = 1, F = 3/2$	$J_{SA}/4$	$(J_{SB}+J_{AB})/4$	0
$F_A = 1, F = 1/2$	$J_{SA}/4$	$-(J_{SB}+J_{AB})/2$	$3\,(J_{SB}-J_{AB})^2/16J_{SA}$
$F_A = 0, F = 1/2$	$-3J_{SA}/4$	0	$-3(J_{SB}-J_{AB})^2/16J_{SA}$

The zero-order energy $E^{(0)}$ and the first-order correction $\Delta^{(1)}$ have a geometric interpretation. These contributions to the energy are eigenvalues of $H_0 \propto \mathbf{S}\cdot\mathbf{I}_A$ and $H_1^{(1)} \propto \mathbf{F}_A\cdot\mathbf{I}_B$, respectively. Since the dot product of two classical vectors is proportional to the cosine of the angle between them, $E^{(0)}$ and $\Delta^{(1)}$ are each associated with the angle between two vectors. Within the zero-order eigenstates, the angle between $\mathbf{S}$ and $\mathbf{I}_A$ remains fixed during the correlated motions of the spins, as does the angle between $\mathbf{F}_A$ and $\mathbf{I}_B$. Note that this interpretation is consistent with the depiction of the spin motion shown in Fig. 1(d).

Several of the results derived to this point can be summarized by expressing H_0 and H_1 in a basis of zero-order eigenstates. From Table I, these states belong to angular-momentum manifolds specified by the quantum numbers F_A and F. Denoting these states by $|F_A, F, m\rangle$, where m is the z component of the total angular momentum, we define basis B by ordering the states lexicographically, in decreasing order of F_A, F, and m:

$$B = \{|1,3/2,3/2\rangle, \ldots |1,3/2,-3/2\rangle, |1,1/2,1/2\rangle, |1,1/2,-1/2\rangle, |0,1/2,1/2\rangle, |0,1/2,-1/2\rangle\}.$$

Expressed in basis B, the strong coupling and the perturbation take the form

$$H_0 = \frac{J_{SA}}{4}\begin{bmatrix} 1 & & & & & & & \\ & 1 & & & & & & \\ & & 1 & & & & & \\ & & & 1 & & & & \\ & & & & 1 & & & \\ & & & & & 1 & & \\ & & & & & & -3 & \\ & & & & & & & -3 \end{bmatrix} \quad (19)$$

and

$$H_1 = \frac{J_{SB}+J_{AB}}{4}\begin{bmatrix} 1 & & & & & & & \\ & 1 & & & & & & \\ & & 1 & & & & & \\ & & & 1 & & & & \\ & & & & -2 & & & \\ & & & & & -2 & & \\ & & & & & & 0 & \\ & & & & & & & 0 \end{bmatrix} - \frac{\sqrt{3}(J_{SB}-J_{AB})}{4}\begin{bmatrix} 0 & & & & & & & \\ & 0 & & & & & & \\ & & 0 & & & & & \\ & & & 0 & & & & \\ & & & & 0 & & 1 & \\ & & & & & 0 & & 1 \\ & & & & 1 & & 0 & \\ & & & & & 1 & & 0 \end{bmatrix}. \tag{20}$$

In Eqs. (19) and (20), zeros that do not lie along the diagonal have been omitted for clarity. The zero-order energies are given by Eq. (19), while the first-order corrections are given by the first term on the right side of Eq. (20). The second term on the right side of Eq. (20) is neglected in a first-order treatment and is responsible for higher order corrections.

The significance of second-order corrections can be estimated by substituting characteristic values of J_{SA}, J_{SB}, and J_{AB} into the formulas for $\Delta^{(2)}$ that appear in Table I. For molecules where S represents a ^{13}C nucleus coupled through a single bond to I_A, with I_B coupled to the other spins through two or more bonds, we can use $J_{SA} \sim 150$ Hz and $(J_{SB} - J_{AB}) \sim 10$ Hz to make the order-of-magnitude estimate $\Delta^{(2)} \sim \pm 0.125$ Hz. Note that shifts of this magnitude are detectable in zero-field experiments,[15,17,18] as illustrated by spectra presented in Secs. III C and IV B.

B. Spin dipole

Motivated by the discussion of Sec. II, we write the spin dipole of Eq. (7) in the form

$$\boldsymbol{\mu} = \frac{\gamma_I - \gamma_S}{2}\hbar(\mathbf{I}_A - \mathbf{S}) + \frac{\gamma_I - \gamma_S}{4}\hbar(\mathbf{I}_B - \mathbf{F}_A) + \frac{3\gamma_I + \gamma_S}{4}\hbar\mathbf{F}. \tag{21}$$

During a period of free evolution under the Hamiltonian H_J, the term proportional to $\mathbf{F}$ in Eq. (21) does not contribute to the oscillations of $\langle\boldsymbol{\mu}(t)\rangle$, since $\mathbf{F}$ commutes with H_J. In considering the frequency components of $\langle\boldsymbol{\mu}(t)\rangle$, we simplify the discussion by dropping the static term and using

$$\boldsymbol{\mu} = \frac{\gamma_I - \gamma_S}{2}\hbar(\mathbf{I}_A - \mathbf{S}) + \frac{\gamma_I - \gamma_S}{4}\hbar(\mathbf{I}_B - \mathbf{F}_A). \tag{22}$$

Figure 2 suggests that the high-frequency oscillations in $\langle\boldsymbol{\mu}(t)\rangle$ involve motion of the components of I_A and S that are "perpendicular to F_A." To formalize this geometric idea, we define operators

$$\mathbf{S}^{\perp} = \mathbf{S} - \mathbf{S}^{\parallel}, \tag{23a}$$

$$\mathbf{I}_A^{\perp} = \mathbf{I}_A - \mathbf{I}_A^{\parallel}. \tag{23b}$$

Note that Eqs. (16) and (17), which were derived by considering the restriction of $\mathbf{S}$ and $\mathbf{I}_A$ to a manifold of F_A, can be considered to define $\mathbf{S}^{\parallel}$ and $\mathbf{I}_A^{\parallel}$ on the full Hilbert space for the three-spin system, and so $\mathbf{S}^{\perp}$ and $\mathbf{I}_A^{\perp}$ are well-defined on the same space. In describing the formal properties of these operators, however, it is convenient to first consider them as defined on the two-spin space spanned by the states $|F_A, m_A\rangle$. Decomposing $\mathbf{S}$ in the form

$$\mathbf{S} = \mathbf{S}^{\parallel} + \mathbf{S}^{\perp}$$

separates its matrix elements into two sets. The matrix elements that couple states belonging to the same manifold of F_A are denoted by $\mathbf{S}^{\parallel}$, while the matrix elements that couple states belonging to different manifolds are denoted by $\mathbf{S}^{\perp}$. The operators $\mathbf{I}_A^{\parallel}$ and $\mathbf{I}_A^{\perp}$ can be described in a similar way.

The geometric model shown in Fig. 3 motivates similar decompositions of $\mathbf{F}_A$ and $\mathbf{I}_B$. Projecting these operators onto the manifolds of F listed in Table I, we obtain

$$\mathbf{F}_A^{\parallel} = \frac{F(F+1) + F_A(F_A+1) - I_B(I_B+1)}{2F(F+1)}\mathbf{F}, \tag{24a}$$

$$\mathbf{I}_B^{\parallel} = \frac{F(F+1) + I_B(I_B+1) - F_A(F_A+1)}{2F(F+1)}\mathbf{F} \tag{24b}$$

and

$$\mathbf{F}_A^{\perp} = \mathbf{F}_A - \mathbf{F}_A^{\parallel}, \tag{25a}$$

$$\mathbf{I}_B^{\perp} = \mathbf{I}_B - \mathbf{I}_B^{\parallel}. \tag{25b}$$

The projections $\mathbf{F}_A^{\parallel}$, $\mathbf{I}_B^{\parallel}$ have nonzero matrix elements only within manifolds of F, while $\mathbf{F}_A^{\perp}$ and $\mathbf{I}_B^{\perp}$ couple states belonging to different manifolds of F.

Simple algebraic manipulations show that

$$\mathbf{I}_A^{\perp} = -\mathbf{S}^{\perp}, \tag{26a}$$

$$\mathbf{I}_B^{\perp} = -\mathbf{F}_A^{\perp}. \tag{26b}$$

Equation (26a) gives formal support for the picture in which the vectors $\mathbf{I}_A$, $\mathbf{S}$, and $\mathbf{F}_A$ form a triangle, as shown in Fig. 1(a), since this picture implies that $\mathbf{I}_A^{\perp} = -\mathbf{S}^{\perp}$, as shown in Fig. 2(a). Similarly, Eq. (26b) is consistent with the visualization shown in Fig. 3(a).

In demonstrating that the high-frequency components of $\langle\boldsymbol{\mu}(t)\rangle$ are formally associated with the motion of $(\mathbf{I}_A^{\perp} - \mathbf{S}^{\perp})$, we first recall that the zero-order eigenstates were obtained by diagonalizing H_1 within subspaces that can be visualized as containing I_B as well as a single manifold of F_A. Low-frequency oscillations correspond to transitions within one of these subspaces, while high-frequency oscillations correspond to transitions between them. Since the operators $\mathbf{I}_B$ and

$\mathbf{F}_A$ have nonzero matrix elements only within a subspace obtained by adding I_B to a given manifold of F_A, the term proportional to $(\mathbf{I}_B - \mathbf{F}_A)$ in Eq. (22) does not contribute to the high-frequency oscillations. Rather, these oscillations are associated with the matrix elements of $(\mathbf{I}_A - \mathbf{S})$ that couple distinct manifolds of F_A. Alternatively stated, the high-frequency spectrum of $\langle \boldsymbol{\mu}(t) \rangle$ is due to the motion of $(\mathbf{I}_A^{\perp} - \mathbf{S}^{\perp})$, as in Figs. 2(b) and 2(c).

Since $\mathbf{S}^{\parallel} = \mathbf{I}_A^{\parallel}$, we have

$$(\mathbf{I}_A - \mathbf{S}) = (\mathbf{I}_A^{\perp} - \mathbf{S}^{\perp}). \tag{27}$$

It follows from Eq. (27) that $(\mathbf{I}_A - \mathbf{S})$ does not contribute to the low-frequency spectrum of $\langle \boldsymbol{\mu}(t) \rangle$, since $\mathbf{I}_A^{\perp}$ and $\mathbf{S}^{\perp}$ have nonzero matrix elements only between states labeled with different values of F_A. Equation (22) thus implies that the low-frequency oscillations of $\langle \boldsymbol{\mu}(t) \rangle$ are associated with matrix elements of $(\mathbf{I}_B - \mathbf{F}_A)$ that couple states of different energy. These matrix elements can be identified with $(\mathbf{I}_B^{\perp} - \mathbf{F}_A^{\perp})$, since the manifolds of F used in defining the projections $\mathbf{I}_B^{\parallel}$, $\mathbf{F}_A^{\parallel}$ are degenerate energy levels. Consistent with Fig. 3(b), the low-frequency oscillations of $\langle \boldsymbol{\mu}(t) \rangle$ can be associated with the motion of $(\mathbf{I}_B^{\perp} - \mathbf{F}_A^{\perp})$.

C. Spectrum

The dipole $\langle \boldsymbol{\mu}(t) \rangle$ can oscillate at the three transition frequencies of the system. The second-order approximations to these frequencies can be obtained from Table I:

$$\begin{aligned}
\nu_1 &= \frac{3}{4}(J_{SB} + J_{AB}) - \frac{3}{16}\frac{(J_{SB} - J_{AB})^2}{J_{SA}}, \\
\nu_2 &= J_{SA} - \frac{1}{2}(J_{SB} + J_{AB}) + \frac{3}{8}\frac{(J_{SB} - J_{AB})^2}{J_{SA}}, \\
\nu_3 &= J_{SA} + \frac{1}{4}(J_{SB} + J_{AB}) + \frac{3}{16}\frac{(J_{SB} - J_{AB})^2}{J_{SA}}.
\end{aligned} \tag{28}$$

The amplitudes and phases of the spectroscopic peaks at frequencies ν_k depend on the methods used to polarize the sample and acquire the spectrum. References 15–18 describe experimental schemes for zero-field spectroscopy based on the use of an atomic magnetometer as a detector. Here we analyze an acquisition protocol where the sample is prepolarized in an applied field along z. After the field is dropped suddenly to zero, $\langle \mu_z(t) \rangle$ is detected during a period of free evolution. Note that it suffices to detect $\langle \mu_z(t) \rangle$, since the symmetry of the initial state and the scalar-coupling Hamiltonian imply that $\langle \mu_x(t) \rangle = \langle \mu_y(t) \rangle = 0$ during the detection period. The observable can therefore be defined as μ_z.

In order to describe the resulting spectrum, we write the density matrix of the polarized spins at the beginning of the detection period as

$$\rho_0 = (I_{A,z} - S_z) + \frac{1}{2}(I_{B,z} - F_{A,z}), \tag{29}$$

where the proportionality constant that characterizes the strength of the polarization has been dropped, together with the contribution of the identity matrix. Equation (29) was obtained by noting that the spin order associated with weak thermal prepolarization is represented by a density matrix proportional to μ_z. As in Eq. (22), we drop the term proportional to F_z, which does not evolve under H_J. Equations (23) and (25) can be used to decompose each spin operator as the sum of a projection and a perpendicular component. Using Eq. (27) to simplify the resulting expression gives

$$\begin{aligned}
\rho_0 = &\left(I_{A,z}^{\perp} - S_z^{\perp}\right) + \frac{1}{2}\left(I_{B,z}^{\perp} - F_{A,z}^{\perp}\right) \\
&+ \frac{1}{2}\left(I_{B,z}^{\parallel} - F_{A,z}^{\parallel}\right).
\end{aligned} \tag{30}$$

Since the only nonzero matrix elements of the operator $(I_{B,z}^{\parallel} - F_{A,z}^{\parallel})$ are within degenerate manifolds of F, this term is static during a period of free evolution, and it can be dropped. A further simplification can be made using Eqs. (26a) and (26b), which give

$$\rho_0 = 2I_{A,z}^{\perp} + I_{B,z}^{\perp}. \tag{31}$$

The spin order represented by Eq. (31) consists of a set of coherences that oscillate during the detection period. Formally, this motion is described by the time-dependent density matrix

$$\rho(t) = \exp(-itH_J)\,\rho_0\,\exp(itH_J), \tag{32}$$

and the resulting dipole oscillations are given by

$$\langle \mu_z(t) \rangle = \mathrm{Tr}\{\mu_z \rho(t)\}. \tag{33}$$

Note that since $\rho_0 \propto \mu_z$, it follows from Eqs. (22), (32), and (33) that the $\langle \mu_z(t) \rangle \propto (\gamma_I - \gamma_S)^2$.

In describing the spectrum of $\langle \mu_z(t) \rangle$, we use a simplified expression for the operator μ_z. Beginning from Eq. (22), we drop the contributions to μ_z that have matrix elements only within degenerate energy levels. Arguments similar to those used in deriving Eq. (31) show that the matrix elements of μ_z relevant for describing the dipole oscillations can be written in the form

$$\mu_z \propto 2I_{A,z}^{\perp} + I_{B,z}^{\perp}, \tag{34}$$

where physical constants have been dropped, since our interest is in the relative amplitudes of the peaks, rather than the absolute amplitudes. From (32)–(34), we obtain

$$\begin{aligned}
\langle \mu_z(t) \rangle \propto\ & 4\,\mathrm{Tr}\left\{I_{A,z}^{\perp} \exp(-itH_J)\, I_{A,z}^{\perp}\, \exp(itH_J)\right\} \\
&+ \mathrm{Tr}\left\{I_{B,z}^{\perp} \exp(-itH_J)\, I_{B,z}^{\perp}\, \exp(itH_J)\right\}.
\end{aligned} \tag{35}$$

In (35), the terms involving $I_{A,z}^{\perp}$ and $I_{B,z}^{\perp}$ represent the high-frequency and low-frequency contributions to the signal, respectively. The amplitude of the low-frequency peak is therefore $|I_{B,z}^{\perp}|^2$, where the norm of an operator T is defined by

$$|T| = \sqrt{\mathrm{Tr}\{T^{\dagger}T\}}.$$

The sum of the amplitudes of the two high-frequency peaks is $4|I_{A,z}^{\perp}|^2$.

The amplitude of the low-frequency peak can be evaluated by exploiting a generalization of the Pythagorean theorem that holds for the two orthogonal components of $I_{B,z}$:

$$|I_{B,z}|^2 = |I_{B,z}^{\parallel}|^2 + |I_{B,z}^{\perp}|^2. \tag{36}$$

Using Eq. (24b), we find that

$$|I^{\parallel}_{B,z}|^2 = \frac{10}{9},$$

and since $|I_{B,z}|^2 = 2$, it follows from Eq. (36) that the amplitude of the low-frequency peak is

$$|I^{\perp}_{B,z}|^2 = 8/9. \tag{37}$$

Similar manipulations show that the sum of the amplitudes of the high-frequency peaks is

$$4|I^{\perp}_{A,z}|^2 = 4. \tag{38}$$

To find the relative amplitudes of the high-frequency peaks, we first use the Clebsch-Gordan coefficients to obtain explicit formulas for the eigenstates: addition of S and I_A gives states $|F_A, m_A\rangle$, and addition of F_A and I_B gives zero-order eigenstates $|F_A, F, m\rangle$. Each high-frequency peak is associated with a pair of energy levels, and the amplitude of the peak can be found by first evaluating the matrix elements of $I_{A,z}$ that couple states within the two levels and then summing the squared norms of these elements. Performing these calculations shows that the ratio of the amplitudes for frequencies ν_2 and ν_3 is 1:2.

In combination with Eqs. (37) and (38), this result implies that the relative amplitudes of the three peaks in the spectrum are 2:3:6. It follows from (35) that the peaks are "in phase," since each of the oscillating components of $\langle \mu_z(t) \rangle$ takes its maximum value at time $t = 0$. These conclusions are illustrated in Fig. 4, which shows the spectrum derived from perturbation theory for an example three-spin system.

An alternative to thermal prepolarization in an applied field is the use of parahydrogen-induced polarization (PHIP) at zero field.[16,17,25] As an example, we consider the reaction shown in Fig. 5, in which parahydrogen is added to dimethyl acetylenedicarboxylate (DMAD) to yield dimethyl maleate (DMM). With ^{13}C present at natural abundance, the reaction

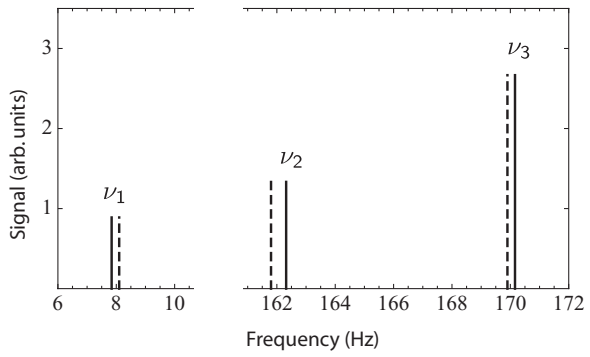

FIG. 4. First-order description (dashed lines) and second-order description (solid lines) of the zero-field spectrum of an example three-spin system. The amplitudes, which were evaluated using zero-order eigenstates, correspond to an experimental protocol in which the molecule is prepolarized in an applied field. After the field is dropped suddenly to zero, the oscillations of the sample dipole are detected. The relative amplitudes of the three peaks are 2:3:6, and the second-order approximations to the frequencies ν_k are given by Eqs. (28), where $J_{SA} = 167.2$ Hz, $J_{SB} = -2.2$ Hz, and $J_{AB} = 13.0$ Hz. These scalar couplings correspond to a system consisting of two ^{1}H nuclei and a ^{13}C nucleus in the vinyl group of dimethyl maleate,[25] shown on the right side of Fig. 5. In this system, the exact transition frequencies differ from the second-order approximations by about 10 mHz.

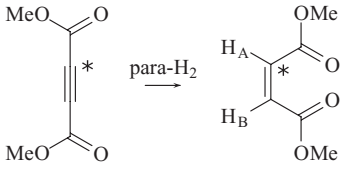

FIG. 5. Hydrogenation of dimethyl acetylenedicarboxylate (DMAD) to form dimethyl maleate (DMM). When the reaction product contains a single ^{13}C nucleus in the vinyl group, the hyperpolarized molecule can be modeled as a three-spin system.

yields a mixture of isotopomers. The signal is primarily generated by isotopomers that have a single ^{13}C nucleus in the vinyl group or in the carboxyl group; for the isotopomer with ^{13}C in the methyl group, the spin order introduced by the addition of parahydrogen is not converted to a detectable signal because the heteronucleus is isolated from the spins of the initial singlet state.[25] The vinyl isotopomer can be modeled as a three-spin system, since the couplings between the vinyl group and the methyl protons are weak. A detailed analysis of the evolution occurring in this isotopomer during the zero-field PHIP experiment predicts that its spectrum contains three peaks of equal amplitude, including a high-frequency antiphase doublet and a single low-frequency peak.[25]

Figure 6 shows the experimental zero-field spectrum for hyperpolarized DMM, together with the first-order description (dashed lines) and second-order description (solid lines) of the spectrum of the vinyl isotopomer. The methods used for the experiment are reported in Ref. 17. The antiphase doublet in the spectrum is associated with the strong single-bond heteronuclear coupling $J_{SA} \approx 170$ Hz in the vinyl isotopomer, and the spacing between the peaks of the doublet is determined by the weak couplings $|J_{SB}|$, $|J_{AB}| \lesssim 10$ Hz. The antiphase peaks have equal integrated area; the small splittings in these peaks are due to weak couplings to the methyl protons,[25] which are not included in the three-spin model of the vinyl isotopomer. The low-frequency region of the spectrum is primarily determined by the carboxyl isotopomer,[25] which can be modeled as a weakly coupled network of six spins, consisting of two vinyl protons, three methyl protons, and the ^{13}C nucleus.

IV. $(XA_n)B_m$ SYSTEMS

Several of the results obtained in Sec. III for the three-spin system can be generalized to systems that contain a heteronucleus and two sets of equivalent protons, with one heteronuclear coupling strong compared to the other couplings. We use the notation $(XA_n)B_m$ to denote this class of spin systems, where X represents the heteronucleus, A_n represents a set of n equivalent protons strongly coupled to X, and B_m represents a set of m equivalent protons weakly coupled to X and A_n. The parentheses group together the strongly coupled spins. The scalar-coupling Hamiltonian H_J has the same form for an $(XA_n)B_m$ system as for the three-spin system of Sec. III, with

$$H_J = H_0 + H_1$$

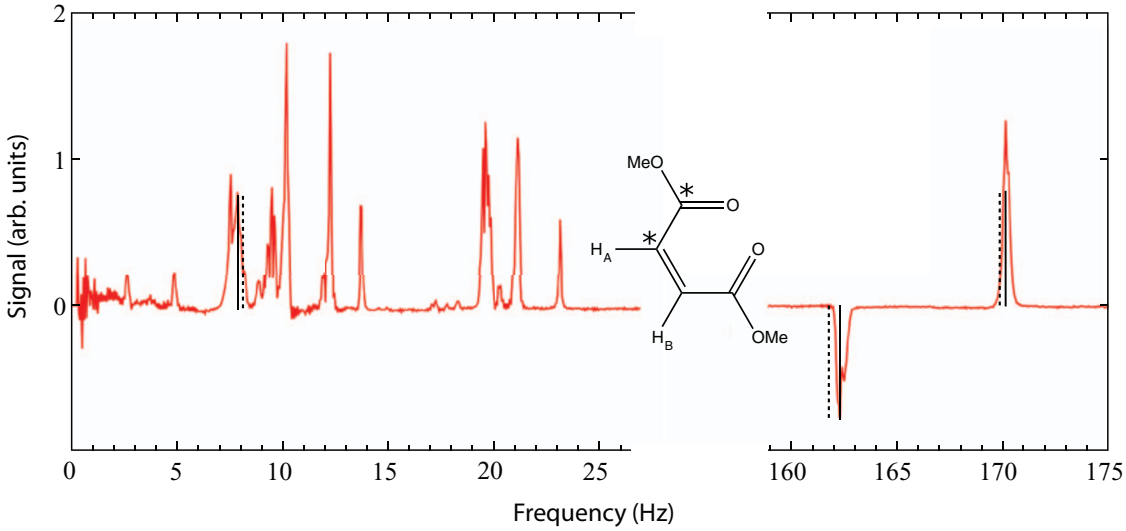

FIG. 6. Zero-field spectrum resulting from the addition of parahydrogen to DMAD to form DMM. The signal is primarily generated by molecules that have a single ^{13}C nucleus in either the vinyl group or the carboxyl group of DMM. The relevant positions of the ^{13}C nucleus are indicated by asterisks in the molecular structure. For the vinyl isotopomer, the first-order description (dashed lines) and second-order description (solid lines) of the spectrum are shown. The transition frequencies were calculated using the coupling constants $J_{SA} = 167.2$ Hz, $J_{SB} = -2.2$ Hz, and $J_{AB} = 13.0$ Hz, as in Fig. 4. The small splittings of the antiphase peaks are due to weak couplings to the methyl protons, which are not included in the three-spin model of the vinyl isotopomer. For the isotopomer with ^{13}C in the carboxyl group, the network of six coupled spins formed by the ^{13}C nucleus, the vinyl protons, and the methyl protons yields a complicated splitting pattern in the low-frequency region of the spectrum.

and

$$\begin{aligned} H_0 &= J_{SA}\,\mathbf{S}\cdot\mathbf{I}_A, \\ H_1 &= J_{SB}\,\mathbf{S}\cdot\mathbf{I}_B + J_{AB}\,\mathbf{I}_A\cdot\mathbf{I}_B. \end{aligned} \tag{39}$$

In Eqs. (39), $\mathbf{I}_A$ and $\mathbf{I}_B$ represent the summed angular momentum of the strongly coupled protons and the weakly coupled protons, respectively.

A. Energy levels

The arguments used in Sec. III A to find the energy levels of a three-spin system can be generalized to an $(XA_n)B_m$ system. For the strongly coupled subsystem XA_n governed by H_0, the eigenstates can be grouped into degenerate manifolds of F_A, the summed angular momentum of the strongly coupled spins.[18] Basis sets that span these manifolds can be obtained by using the Clebsch-Gordan coefficients to add the angular momenta S and I_A. Algebraic manipulations similar to those performed in deriving Eqs. (15) and (18) show that for each manifold, the zero-order energy is[18]

$$\begin{aligned} E^{(0)} = \frac{J_{SA}}{2}[&F_A(F_A+1) - S(S+1) \\ &- I_A(I_A+1)]. \end{aligned} \tag{40}$$

The degenerate eigenspaces of H_0 consist of states $|F_A, m_A\rangle|\psi\rangle$, where $|\psi\rangle$ is a state of the weakly coupled spins. An $(XA_n)B_m$ system differs formally from the three-spin system in that an eigenspace of H_0 cannot in general be associated with a unique manifold of states $|F_A, m_A\rangle$. We wish to establish that within each eigenspace, the operators $\mathbf{S}$ and $\mathbf{I}_A$ can be replaced by their projections onto individual manifolds of F_A, which implies that the first-order approximation to H_1 has the form given by Eq. (4):

$$H_1^{(1)} = J_{SB}\,\mathbf{S}^{\|}\cdot\mathbf{I}_B + J_{AB}\,\mathbf{I}_A^{\|}\cdot\mathbf{I}_B. \tag{41}$$

In Eq. (41), $\mathbf{S}^{\|}$ and $\mathbf{I}_A^{\|}$ are defined by Eqs. (16) and (17), respectively.

As an example, we consider an XA_3 subsystem. The three equivalent protons yield a set of three manifolds of I_A, with I_A taking the values 1/2, 1/2, and 3/2. Because of the presence of two manifolds with $I_A = 1/2$, the manifolds of F_A obtained by adding S and I_A include pairs that have the same quantum numbers S, $I_A = 1/2$, F_A, and the same energy $E^{(0)}$. However, these pairs are not coupled by the operators $\mathbf{S}$ and $\mathbf{I}_A$, which have nonzero matrix elements only within subspaces V obtained by adding S to a single manifold of I_A. Each subspace V is spanned by a set of manifolds labeled with distinct values of F_A, and Eq. (40) implies that these manifolds have distinct energies $E^{(0)}$. It follows that in every case where a pair of states that belong to different manifolds of F_A is coupled by $\mathbf{S}$ or $\mathbf{I}_A$, the zero-order energies of the two states are different. Within the degenerate eigenspaces of H_0, the operators $\mathbf{S}$ and $\mathbf{I}_A$ can thus be replaced by projections onto individual manifolds of F_A. The same conclusion holds for an XA_n subsystem.

For an $(XA_n)B_m$ system, the subspaces within which H_1 must be diagonalized can be visualized as containing a single spin F_A that interacts with the weakly coupled spins through a scalar coupling $\mathbf{F}_A\cdot\mathbf{I}_B$. Formally, these subspaces are the product of a manifold of F_A and the state space of the weakly coupled spins. In a given subspace, the perturbation can be written as

$$H_1^{(1)} = \left(J_{SB}^{\|} + J_{AB}^{\|}\right)\mathbf{F}_A\cdot\mathbf{I}_B, \tag{42}$$

where

$$J_{SB}^{\parallel} = J_{SB} \times \frac{F_A(F_A+1)+S(S+1)-I_A(I_A+1)}{2F_A(F_A+1)},$$
$$J_{AB}^{\parallel} = J_{AB} \times \frac{F_A(F_A+1)+I_A(I_A+1)-S(S+1)}{2F_A(F_A+1)} \quad (43)$$

are couplings scaled by the projection of $\mathbf{S}$ and $\mathbf{I}_A$ onto $\mathbf{F}_A$. The energy levels of $H_1^{(1)}$ can be found by adding F_A and I_B to obtain manifolds labeled with the quantum numbers S, I_A, F_A, I_B, and F. Manipulations similar to those performed in deriving Eqs. (15) and (18) show that first-order energy correction in each of these manifolds is

$$\Delta^{(1)} = \frac{1}{2}\left(J_{SB}^{\parallel} + J_{AB}^{\parallel}\right) \times [F(F+1) - F_A(F_A+1) - I_B(I_B+1)]. \quad (44)$$

The second-order energy corrections can be evaluated using formulas derived in the Appendix.

B. Spectrum

The description of the oscillating spin dipole given in Sec. III B for the three-spin system applies also to the $(XA_n)B_m$ system, with the exception of Eq. (27), which holds only when $\mathbf{S}^{\parallel} = \mathbf{I}_A^{\parallel}$ or, equivalently, when $S = I_A$. Arguments similar to those presented in Sec. III B show that the high-frequency oscillations of $\langle \boldsymbol{\mu}(t) \rangle$ are associated with the motion of $(\mathbf{I}_A^{\perp} - \mathbf{S}^{\perp})$. The low-frequency oscillations can in general include contributions both from $(\mathbf{I}_B^{\perp} - \mathbf{F}_A^{\perp})$ and from the projections of $\mathbf{S}$ and $\mathbf{I}_A$ onto $\mathbf{F}_A$.

In the case where the spins are prepolarized by thermal equilibration in an applied field, the initial density matrix can be written in the form

$$\rho_0 = (I_{A,z} - S_z) + \frac{1}{2}(I_{B,z} - F_{A,z}),$$

as in Eq. (29). Decomposing each spin operator as the sum of a projection and a perpendicular component yields

$$\rho_0 = \left(I_{A,z}^{\perp} - S_z^{\perp}\right) + \left(I_{A,z}^{\parallel} - S_z^{\parallel}\right) + \frac{1}{2}\left(I_{B,z}^{\perp} - F_{A,z}^{\perp}\right) + \frac{1}{2}\left(I_{B,z}^{\parallel} - F_{A,z}^{\parallel}\right),$$

which differs from Eq. (30) due to the fact that Eq. (27) does not hold. Dropping the static term $(I_{B,z}^{\parallel} - F_{A,z}^{\parallel})$ and taking account of Eqs. (26a) and (26b) gives

$$\rho_0 = 2I_{A,z}^{\perp} + I_{B,z}^{\perp} + \left(I_{A,z}^{\parallel} - S_z^{\parallel}\right). \quad (45)$$

On the right side of Eq. (45), the term $2I_{A,z}^{\perp}$ is responsible for the high-frequency dipole oscillations, while the remaining terms can contribute to the low-frequency oscillations. The operators $I_{A,z}^{\perp}$ and $I_{B,z}^{\perp}$ represent a set of coherences that oscillate during free evolution, while the operator $(I_{A,z}^{\parallel} - S_z^{\parallel})$ in general includes both coherences and nonzero matrix elements within degenerate manifolds of F.

The selection rules,

$$\Delta F = 0, \pm 1, \quad (46a)$$

$$\Delta F_A = \pm 1, \quad (46b)$$

$$\Delta I_A = 0, \quad (46c)$$

$$\Delta I_B = 0, \quad (46d)$$

limit the transition frequencies that can appear in the high-frequency spectrum. Equation (46a) follows from the Wigner-Eckart theorem, since $I_{A,z}$ is a component of a vector operator, while Eqs. (46c) and (46d) are due to the fact that $I_{A,z}$ commutes with $\mathbf{I}_A^2$ and $\mathbf{I}_B^2$, respectively. To derive Eq. (46b), we consider the matrix elements of $I_{A,z}$ within the XA_n subsystem. These are confined to subspaces V obtained by adding S to a single manifold of I_A, which yields manifolds

$$F_A = |I_A - S|, \ldots, |I_A + S|, \quad (47)$$

each with a distinct energy $E^{(0)}$. Because $I_{A,z}$ is a component of a vector operator, its matrix elements within a subspace V satisfy the selection rule $\Delta F_A = 0, \pm 1$. Since the manifolds listed in (47) all have distinct values of F_A, a transition within V represented by $I_{A,z}$ must have $\Delta F_A = \pm 1$. The same selection rule holds for the high-frequency transitions between eigenstates obtained by adding F_A and I_B.

In determining the selection rules for the low-frequency transitions, we recall that these transitions occur within degenerate eigenspaces of H_0. It follows from the discussion in Sec. IV A that within each of these eigenspaces, the nonzero matrix elements of $I_{A,z}$, $I_{B,z}$, and S_z are confined to subspaces W obtained by adding a single manifold of F_A to a single manifold of I_B. The selection rule

$$\Delta F_A = 0$$

is a consequence of this restriction. The selection rules given by Eqs. (46a), (46c), and (46d) apply also to the low-frequency peaks, because of properties of $I_{B,z}$ and S_z analogous to those of $I_{A,z}$.

The choice to define the axis of the initial spin polarization as the z axis yields the additional selection rule

$$\Delta m = 0, \quad (48)$$

where m is the z component of the total angular momentum. As noted in Sec. III C, the symmetry of the initial state and the scalar-coupling Hamiltonian imply that $\langle \mu_x(t) \rangle = \langle \mu_y(t) \rangle = 0$ during the detection period, and so the observable can be defined as μ_z. Since the observable is the z component of a vector operator, Eq. (48) follows from the Wigner-Eckart theorem, and it applies to all transitions in the spectrum.

For the three-spin system prepolarized by thermal equilibration in an applied field, Eq. (31) gives a compact expression for the coherences in the initial density matrix. An analogous expression can be derived for $(XA_n)B_m$ systems. Within a subspace W obtained by adding a manifold of F_A to a manifold of I_B, the operator $(I_{A,z}^{\parallel} - S_z^{\parallel})$ appearing in Eq. (45) is proportional to $F_{A,z}$:

$$\left(I_{A,z}^{\parallel} - S_z^{\parallel}\right) = \frac{I_A(I_A+1) - S(S+1)}{F_A(F_A+1)} F_{A,z}. \quad (49)$$

Note that the quantum numbers I_A and F_A have well-defined values within each subspace W. We decompose $F_{A,z}$ in

Eq. (49) as the sum of $F^{\parallel}_{A,z}$ and $F^{\perp}_{A,z}$, and we drop the static term $F^{\parallel}_{A,z}$. Substitution into Eq. (45) gives

$$\rho_0 = 2I^{\perp}_{A,z} + I^{\perp}_{B,z} + \frac{I_A(I_A+1) - S(S+1)}{F_A(F_A+1)} F^{\perp}_{A,z} \tag{50a}$$

$$= 2I^{\perp}_{A,z} + \left[1 - \frac{I_A(I_A+1) - S(S+1)}{F_A(F_A+1)}\right] I^{\perp}_{B,z}, \tag{50b}$$

where the second line follows from Eq. (26b). The terms proportional to $I^{\perp}_{A,z}$ and $I^{\perp}_{B,z}$ in Eq. (50b) represent high-frequency and low-frequency coherences, respectively. The coefficient of $I^{\perp}_{B,z}$ in Eq. (50b) depends on the values of I_A and F_A for the states involved in a given low-frequency coherence. The relative amplitudes of the peaks in the spectrum can be evaluated using Eq. (50a) or (50b). For a given pair of energy levels, the amplitude of the corresponding peak is found by summing the squared norms of the matrix elements of ρ_0 that represent coherences between states belonging to the two levels.

Reference 45 discusses the analysis of zero-field spectra for $(XA_n)B_m$ systems and shows several experimental examples. For the present discussion, we consider the spectrum of labeled methyl formate ($H^{13}COOCH_3$) prepolarized by thermal equilibration in an applied field. Figure 7(a) shows an experimental spectrum acquired using previously reported methods,[15,18] together with the first-order description (dashed lines) and the second-order description (solid lines) of the spectrum. The labeled carbon atom of the formyl group is directly bonded to a single hydrogen atom; in the absence of couplings to the methyl protons, the nuclei of these two atoms would form a strongly coupled XA system. The single transition that can occur in such a system is shown in Fig. 7(b). Due to the presence of weak couplings between the methyl protons and the spins of the formyl group, methyl formate is

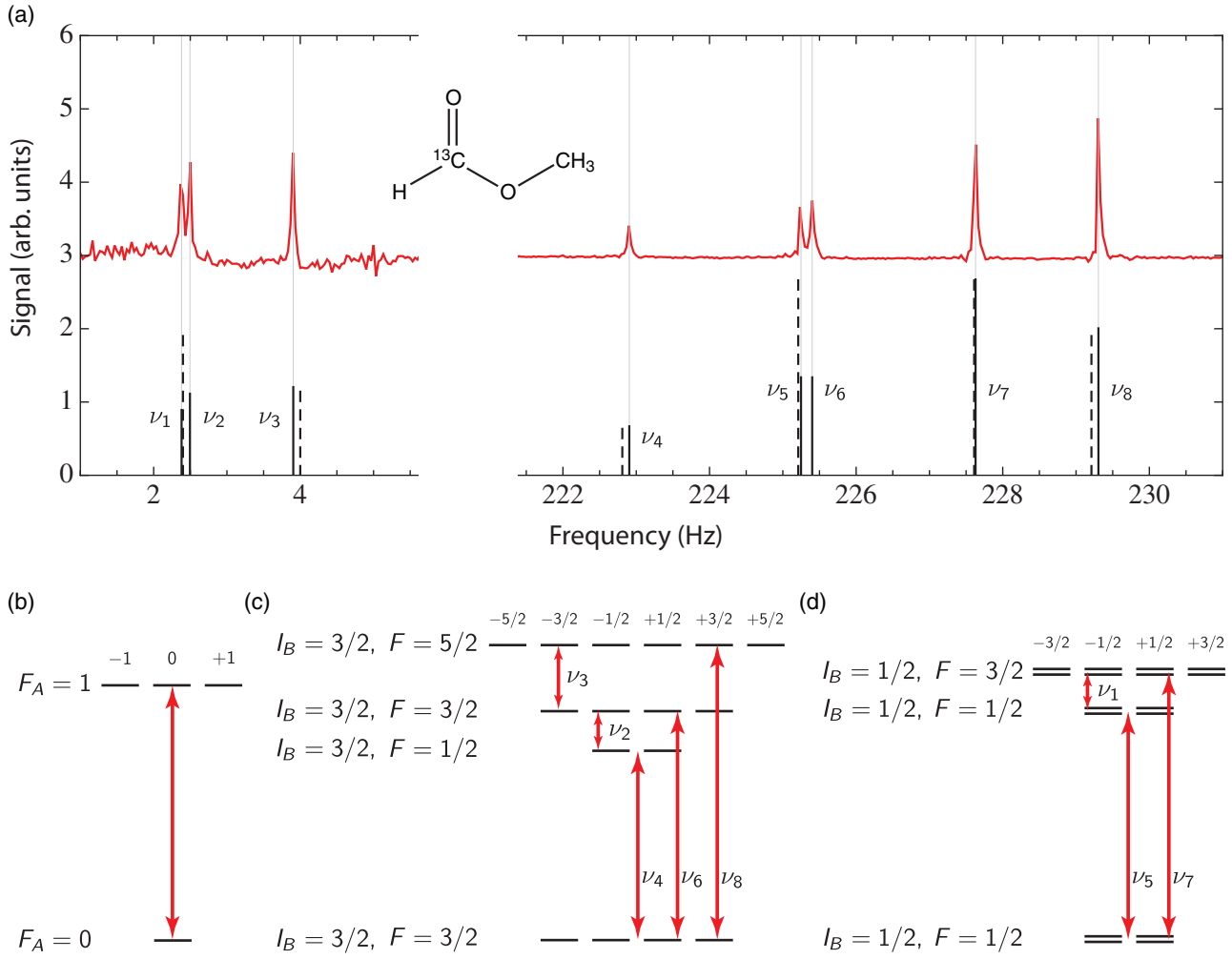

FIG. 7. Zero-field spectrum and allowed transitions of labeled methyl formate ($H^{13}COOCH_3$) prepolarized by thermal equilibration in an applied field. The molecule is an $(XA)B_3$ system, where X and A correspond to the ^{13}C nucleus and the ^{1}H nucleus of the formyl group, respectively, and where the weakly coupled spins represented by B_3 are the ^{1}H nuclei of the methyl group. (a) The trace shows the experimental spectrum, while the dashed lines and the solid lines show the first-order description and second-order description of the spectrum, respectively. Amplitudes were calculated using zero-order eigenstates. For the second-order description of the spectrum, the relative amplitudes of the peaks in the high-frequency multiplet are 1:2:2:4:3, while the relative amplitudes of the eight peaks in the full spectrum are 20:25:27:15:30:30:60:45. The scalar couplings used for the calculations were $^{1}J_{SA} = 226.81$ Hz, $^{3}J_{SB} = 4.0$ Hz, and $^{4}J_{AB} = -0.8$ Hz, chosen by finding a visual match between exact simulations and the experimental data. (b) Energy levels and allowed transition for a strongly coupled XA system. (c) Energy levels and transitions within the subspace obtained by adding F_A to $I_B = 3/2$. (d) Energy levels and transitions within the subspace obtained by adding F_A to the two manifolds with $I_B = 1/2$. The closely spaced energy states are degenerate. In (c) and (d), arrows showing allowed transitions specify pairs of energy levels involved in a transition.

TABLE II. Approximate energy levels of labeled methyl formate ($H^{13}COOCH_3$), an $(XA)B_3$ system. The eigenstates can be grouped into degenerate angular-momentum manifolds labeled with quantum numbers S, I_A, F_A, I_B, and F. All of the manifolds have $S = I_A = 1/2$. The values of F_A, I_B, and F are shown in the table, along with the zero-order energy $E^{(0)}$ and the energy corrections $\Delta^{(1)}$, $\Delta^{(2)}$. For energy levels with $F_A = 0$, the first-order correction is zero, since the projections of $\mathbf{S}$ and $\mathbf{I}_A$ onto $\mathbf{F}_A$ are zero. As shown in the Appendix, second-order energy corrections in $(XA_n)B_m$ systems are due to couplings between states that have the same values of I_A, I_B, and F but distinct zero-order energies. For the energy levels in the table that have $\Delta^{(2)} = 0$, the zero-order energy is uniquely specified by the values of I_A, I_B, and F.

Angular momenta	$E^{(0)}$	$\Delta^{(1)}$	$\Delta^{(2)}$
$F_A = 1, I_B = 3/2, F = 5/2$	$J_{SA}/4$	$3(J_{SB} + J_{AB})/4$	0
$F_A = 1, I_B = 3/2, F = 3/2$	$J_{SA}/4$	$-(J_{SB} + J_{AB})/2$	$15(J_{SB} - J_{AB})^2/16J_{SA}$
$F_A = 1, I_B = 3/2, F = 1/2$	$J_{SA}/4$	$-5(J_{SB} + J_{AB})/4$	0
$F_A = 1, I_B = 1/2, F = 3/2$	$J_{SA}/4$	$(J_{SB} + J_{AB})/4$	0
$F_A = 1, I_B = 1/2, F = 1/2$	$J_{SA}/4$	$-(J_{SB} + J_{AB})/2$	$3(J_{SB} - J_{AB})^2/16J_{SA}$
$F_A = 0, I_B = 3/2, F = 3/2$	$-3J_{SA}/4$	0	$-15(J_{SB} - J_{AB})^2/16J_{SA}$
$F_A = 0, I_B = 1/2, F = 1/2$	$-3J_{SA}/4$	0	$-3(J_{SB} - J_{AB})^2/16J_{SA}$

an $(XA)B_3$ system. The energy levels and allowed transitions are shown in Figs. 7(c) and 7(d). The zero-order eigenstates are found by adding the angular momenta F_A and I_B to form manifolds of F. Because there are three equivalent protons in the methyl group, I_B takes the values 1/2, 1/2, and 3/2. Figure 7(c) shows the manifolds of F obtained by adding F_A to $I_B = 3/2$, while Fig. 7(d) shows the manifolds obtained by adding F_A to the two manifolds with $I_B = 1/2$. The allowed transitions are represented by arrows, each of which specifies a pair of energy levels involved in a transition.

The first-order and second-order approximations to the transition frequencies can be obtained from Table II. The formulas for $E^{(0)}$ and $\Delta^{(1)}$ given in the table were obtained from Eqs. (40) and (44), respectively, while the second-order corrections were evaluated as described in the Appendix. Examination of the table shows that the transition frequencies denoted by ν_5 and ν_6 in Fig. 7 are degenerate to first order, but the degeneracy is lifted by second-order energy corrections. Similarly, the degeneracy between frequencies ν_1 and ν_2 is lifted by second-order corrections. These second-order splittings can be observed in the experimental spectrum; each is associated with a pair of closely spaced peaks. Note that the peaks at frequencies ν_1 and ν_2 are well resolved, although they are separated by only 0.1 Hz.

V. STRONGLY COUPLED AND WEAKLY COUPLED SUBSYSTEMS

The formal geometric description of zero-field spin motion given in Secs. III and IV is based on the use of the projection theorem to find a truncated Hamiltonian for weak scalar couplings. Because of the generality of the projection theorem, a broad range of scalar-coupled networks can be described in a similar way. As an example, we consider the case where the spins can be divided into a strongly coupled set A and a weakly coupled set B. The Hamiltonian H_0 governs the interactions within set A, and the perturbation H_1 couples the spins of set A to the spins of set B, as well as governing the interactions within set B. Because of the spherical symmetry of the scalar-coupling Hamiltonian, the energy eigenstates of set A under H_0 can be grouped into degenerate manifolds of F_A, the summed angular momentum of the spins in set A. For simplicity, we assume that the energies of these manifolds under H_0 are widely spaced.

We consider a weak scalar coupling between spin I_a belonging to A and spin I_b belonging to B:

$$H_{ab} = J_{ab}\mathbf{I}_a \cdot \mathbf{I}_b.$$

The first-order approximation to the coupling is given by the restriction of H_{ab} to the degenerate eigenspaces of H_0, which consist of states $|F_A, m_A\rangle|\psi\rangle$, where $|\psi\rangle$ is a state function for the spins of set B. As in Eq. (10), a matrix element of H_{ab} between states that belong to a degenerate eigenspace of H_0 has the form

$$J_{ab}\,\langle\psi|\langle F_A, m_A|\,\mathbf{I}_a \cdot \mathbf{I}_b\,|F_A, m'_A\rangle|\psi'\rangle = J_{ab}\,\langle F_A, m_A|\mathbf{I}_a|F_A, m'_A\rangle \cdot \langle\psi|\mathbf{I}_b|\psi'\rangle.$$

Using the projection theorem,[48] we write

$$J_{ab}\langle F_A, m_A|\mathbf{I}_a|F_A, m'_A\rangle = J_{ab}\langle F_A, m_A|\mathbf{I}_a^{\parallel}|F_A, m'_A\rangle = J_{ab}^{\parallel}\langle F_A, m_A|\mathbf{F}_A|F_A, m'_A\rangle,$$

where

$$\mathbf{I}_a^{\parallel} = \frac{\langle \mathbf{I}_a \cdot \mathbf{F}_A\rangle}{\langle \mathbf{F}_A \cdot \mathbf{F}_A\rangle}\mathbf{F}_A \tag{51}$$

is the projection of $\mathbf{I}_a$ onto the manifold of states $|F_A, m_A\rangle$, and where

$$J_{ab}^{\parallel} = \frac{\langle \mathbf{I}_a \cdot \mathbf{F}_A\rangle}{\langle \mathbf{F}_A \cdot \mathbf{F}_A\rangle}J_{ab}$$

is the scaled coupling constant for the truncated interaction that survives averaging by H_0. To first order, the weak coupling can be thus be approximated as

$$H_{ab}^{(1)} = J_{ab}^{\parallel}\mathbf{F}_A \cdot \mathbf{I}_b. \tag{52}$$

As in the geometric model of Sec. II, averaging over the fast evolution governed by H_0 projects the strongly coupled spins onto $\mathbf{F}_A$.

Each degenerate eigenspace of H_0 can be visualized as containing a spin F_A that interacts with the weakly coupled spins of set B. The simplification associated with the use of

first-order perturbation theory is to replace the set of strongly coupled spins by a series of individual spins F_A, each of which interacts with the spins of set B in a separate subspace. Within one of these subspaces, the coupling constant for the interaction between F_A and a given spin I_b of set B is

$$J^{\parallel}_{Ab} = \sum_{I_a \in A} J^{\parallel}_{ab}.$$

Note that in general, the scaled couplings $J^{\parallel}_{ab}$ take distinct values in distinct subspaces, as illustrated by Eqs. (43). Diagonalizing H_1 within each subspace yields zero-order eigenstates and first-order energies. These eigenstates can be grouped into degenerate manifolds of the total angular momentum F.

To generalize the description of the dipole oscillations given in Sec. III B, we write the spin dipole as

$$\boldsymbol{\mu} = \boldsymbol{\mu}_A + \boldsymbol{\mu}_B,$$

where

$$\boldsymbol{\mu}_A = \sum_{I_a \in A} \gamma_a \hbar \mathbf{I}_a, \tag{53a}$$

$$\boldsymbol{\mu}_B = \sum_{I_b \in B} \gamma_b \hbar \mathbf{I}_b, \tag{53b}$$

with γ_k the gyromagnetic ratio for spin I_k. If the spins in set A all have the same gyromagnetic ratio, then $\boldsymbol{\mu}_A \propto \mathbf{F}_A$ does not evolve under H_0. When set A includes more than one nuclear species, however, the fast spin motion governed by H_0 in general causes $\boldsymbol{\mu}_A$ to evolve. Generalizing Eqs. (23a) and (23b), we decompose the vector operator for each strongly coupled spin as a sum of orthogonal components,

$$\mathbf{I}_a = \mathbf{I}^{\parallel}_a + \mathbf{I}^{\perp}_a,$$

where $\mathbf{I}^{\parallel}_a$ is defined by Eq. (51). Arguments similar to those presented in Sec. III B show that the high-frequency oscillations of the molecular spin dipole are due to the motion of the components $\mathbf{I}^{\perp}_a$, which are "perpendicular to $\mathbf{F}_A$." The fast motion of these components is modulated by the slow evolution of $\mathbf{F}_A$ under the effective Hamiltonian $H^{(1)}_1$, which includes truncated couplings of the form given by Eq. (52) as well as couplings between the spins of set B. This modulation yields multiplets in the high-frequency range of the spectrum.

Low-frequency peaks are due to the motion of $\mathbf{F}_A$ and the spins in set B. To demonstrate this, we note that the transitions associated with these peaks occur within subspaces W that are degenerate under H_0. Within a given subspace W, each operator $\mathbf{I}_a$ that represents a strongly coupled spin is proportional to $\mathbf{F}_A$. From Eq. (53a), it follows that $\boldsymbol{\mu}_A \propto \mathbf{F}_A$ within W, and we write

$$\boldsymbol{\mu} = \gamma_A \hbar \mathbf{F}_A + \sum_{I_b \in B} \gamma_b \hbar \mathbf{I}_b,$$

where γ_A is an effective gyromagnetic ratio associated with the subspace W. For homonuclear spin systems, the gyromagnetic ratios for the weakly coupled spins are all equal to γ_A, and $\boldsymbol{\mu} \propto \mathbf{F}$ does not evolve under $H^{(1)}_1$. For spin systems containing more than one nuclear species, the slow evolution of $\mathbf{F}_A$ and the weakly coupled spins in general yields low-frequency dipole oscillations. Equations (24) and (25) can be generalized by projecting $\mathbf{F}_A$ and $\mathbf{I}_b$ onto the degenerate manifolds of F within W. The low-frequency spectrum of $\langle \boldsymbol{\mu}(t) \rangle$ can then be identified with the motion of the components $\mathbf{F}^{\perp}_A$, $\mathbf{I}^{\perp}_b$ that are "perpendicular to $\mathbf{F}$," as in the geometric model.

VI. CONCLUSION

We have used the projection theorem to give a geometric description of zero-field spin systems with truncated scalar couplings. As in the vector model of the atom,[46,47] spins are visualized as classical vectors that precess under the scalar-coupling Hamiltonian. For a three-spin system containing a single strong coupling between $\mathbf{S}$ and $\mathbf{I}_A$, the strong coupling causes the two spins to precess about their summed angular momentum $\mathbf{F}_A$. In the absence of additional couplings, $\mathbf{F}_A$ is motionless. If $\mathbf{S}$ and $\mathbf{I}_A$ are weakly coupled to a third spin $\mathbf{I}_B$, it does not "see" the instantaneous states of the two strongly coupled spins; rather it effectively interacts with the projections of $\mathbf{S}$ and $\mathbf{I}_A$ onto $\mathbf{F}_A$. These projections represent an average over the fast evolution. The truncated weak interactions cause $\mathbf{F}_A$ and $\mathbf{I}_B$ to precess slowly about $\mathbf{F}$, the total angular momentum.

If the gyromagnetic ratios of $\mathbf{S}$ and $\mathbf{I}_A$ are different, their fast precession about $\mathbf{F}_A$ causes oscillations in the molecular spin dipole, detectable as a high-frequency peak in the zero-field spectrum. The modulation of this fast motion by the slow evolution of $\mathbf{F}_A$ splits the peak into a doublet. The precession of $\mathbf{F}_A$ and $\mathbf{I}_B$ about $\mathbf{F}$ yields a single low-frequency peak.

This geometric description can be generalized to a range of zero-field spin systems, including $(XA_n)B_m$ systems, which contain a heteronucleus and two sets of equivalent protons, with one set of protons strongly coupled to the heteronucleus. For spin systems that consist of a strongly coupled heteronuclear subsystem A and a weakly coupled subsystem B, the zero-field spectrum contains high-frequency peaks associated with the motion of the strongly coupled spins $\mathbf{I}_a$. These peaks are split into multiplets because the motion of the spins $\mathbf{I}_a$ is modulated by the slow evolution of $\mathbf{F}_A$, the summed angular momentum of the spins in A. This slow evolution is due to truncated weak couplings that act between $\mathbf{F}_A$ and the spins $\mathbf{I}_b$ belonging to subsystem B. Since the effective gyromagnetic ratio for $\mathbf{F}_A$ is different than the gyromagnetic ratios of the weakly coupled spins $\mathbf{I}_b$, the motion of $\mathbf{F}_A$ and the spins $\mathbf{I}_b$ yields low-frequency multiplets.

The experimental spectra presented here show significant second-order shifts in organic molecules for which H_0 represents a single-bond heteronuclear coupling and H_1 represents couplings that act through two or more bonds. In particular, the spectrum of singly labeled methyl formate shows that a pair of transitions which are degenerate to first order can be separated by second-order energy shifts, yielding a pair of closely spaced peaks in the spectrum. First-order and second-order energy shifts for $(XA_n)B_m$ systems can be obtained from analytic formulas, which facilitates peak assignment and precise determination of the couplings.

ACKNOWLEDGMENTS

Research was supported by the U.S. Department of Energy, Office of Basic Energy Sciences, Division of Materials Sciences and Engineering under Contract No. DE-AC02-05CH11231 [theoretical work, salaries for T. Theis, J. Blanchard, A. Pines], and by the National Science Foundation under Award No. CHE-095765 [zero-field experiments and instrumentation, salaries for M. Butler, M. Ledbetter, D. Budker, A. Pines]. J. Blanchard is supported by a National Science Foundation Graduate Research Fellowship under Grant No. DGE-1106400. We thank Professor Marcis Auzinsh for comments on the manuscript.

APPENDIX: SECOND-ORDER ENERGY CORRECTIONS

As illustrated by Figs. 6 and 7, first-order approximations to the transition frequencies in organic molecules are inadequate for reproducing experimental spectra. For $(XA_n)B_m$ systems, introduced in Sec. IV, analytic formulas for the second-order energy corrections $\Delta^{(2)}$ can be derived. As we show below, $\Delta^{(2)}$ can be evaluated by using the Wigner 6*j*-symbols to express the zero-order eigenstates in basis sets where the operators representing the weak scalar couplings are diagonal. In particular, the second-order corrections shown in Tables I and II were obtained in this way.

The discussion in Sec. IV shows that zero-order eigenstates are found by first adding S and I_A to obtain manifolds of F_A, and then adding F_A and I_B to obtain degenerate manifolds of F. Adding the angular momenta in this order yields a basis set in which the operator $\mathbf{S}\cdot\mathbf{I}_A$ is diagonal; indeed, algebraic manipulations similar to those performed in deriving Eqs. (15) and (18) show that

$$\langle \mathbf{S}\cdot\mathbf{I}_A\rangle = \frac{1}{2}[F_A(F_A+1) - S(S+1) - I_A(I_A+1)].$$

Adding S, I_A, and I_B in a different order yields a basis set in which a different scalar coupling is diagonal. If S and I_B are added first, for example, we obtain manifolds labeled with F_B, the summed angular momentum of S and I_B. The operator $\mathbf{S}\cdot\mathbf{I}_B$ is diagonal in the resulting basis set, with

$$\langle \mathbf{S}\cdot\mathbf{I}_B\rangle = \frac{1}{2}[F_B(F_B+1) - S(S+1) - I_B(I_B+1)].$$

Similarly, if I_A and I_B are added first, the resulting basis states are eigenstates of the operator $\mathbf{I}_A\cdot\mathbf{I}_B$.

The 6*j* symbols can be used to perform the transformation between basis sets obtained by adding the three angular momenta in a different order. Consider a subspace X obtained by adding single manifolds of S, I_A, and I_B. Regardless of the order in which the angular momenta are added, the resulting states can be labeled with the quantum numbers S, I_A, I_B, F, and m, the z component of the total angular momentum. If S and I_A are added first, the states can also be labeled with quantum number F_A, while if S and I_B are added first, the states can be labeled with F_B. Since the values of S, I_A, and I_B are the same for all states in X, we simplify notation by dropping these quantum numbers, so that states labeled with F_A and F_B are denoted by $|F_A, F, m\rangle$ and $|F_B, F, m\rangle$, respectively. The sets $\{|F_A, F, m\rangle\}$ and $\{|F_B, F, m\rangle\}$ each form a basis set for X, and the transformation between these bases is given by[49]

$$\begin{aligned}\langle F_B, F', m' \mid F_A, F, m\rangle &= \delta_{F,F'}\,\delta_{m,m'}\,(-1)^{S+I_A+I_B+F} \\ &\times \sqrt{(2F_A+1)(2F_B+1)} \\ &\times \begin{Bmatrix} S & I_B & F_B \\ F & I_A & F_A \end{Bmatrix}, \end{aligned} \tag{A1}$$

where the quantity delimited by curly brackets is a 6*j* symbol.

To evaluate the second-order energy corrections, we note first the H_1 has nonzero matrix elements only within the subspaces X defined in the previous paragraph. Since it is a scalar operator, the Wigner-Eckart theorem implies that it introduces couplings only between states labeled with the same values of F and m. In taking account of the matrix elements of H_1 that were neglected in the first-order approximation to the energies, we can thus limit our consideration to subspaces Y, each spanned by a set of states $|F_A, F, m\rangle$ that have the same values of F and m but distinct values of F_A. From Eq. (40), the zero-order energies of these states are distinct, and so perturbation theory for nondegenerate states can be used to evaluate energy corrections.

We let $|\phi_p\rangle$ denote a given state $|F_A, F, m\rangle$, and we evaluate the sum

$$\Delta_p^{(2)} = \sum_{q\neq p} \frac{|\langle\phi_p|H_1|\phi_q\rangle|^2}{E_p^{(0)} - E_q^{(0)}}, \tag{A2}$$

where the sum is over the states $\phi_q = |F_A', F, m\rangle$ that belong to the same subspace Y as ϕ_p. We write the matrix element $\langle\phi_p|H_1|\phi_q\rangle$ in the form

$$J_{SB}\langle\phi_p|\mathbf{S}\cdot\mathbf{I}_B|\phi_q\rangle + J_{AB}\langle\phi_p|\mathbf{I}_A\cdot\mathbf{I}_B|\phi_q\rangle,$$

and we consider first the term $\langle\phi_p|\mathbf{S}\cdot\mathbf{I}_B|\phi_q\rangle$. Equation (A1) can be used to express $|\phi_p\rangle$ and $|\phi_q\rangle$ in the basis set where the operator $\mathbf{S}\cdot\mathbf{I}_B$ is diagonal, which gives

$$\begin{aligned}\langle\phi_p|\mathbf{S}\cdot\mathbf{I}_B|\phi_q\rangle = &\sum_{F_B=|S-I_B|}^{|S+I_B|} \left(F_B+\frac{1}{2}\right)\sqrt{(2F_A+1)(2F_A'+1)} \\ &\times \begin{Bmatrix} S & I_B & F_B \\ F & I_A & F_A \end{Bmatrix}\begin{Bmatrix} S & I_B & F_B \\ F & I_A & F_A' \end{Bmatrix} \\ &\times [F_B(F_B+1) - S(S+1) - I_B(I_B+1)]. \end{aligned} \tag{A3}$$

Similarly, we find that

$$\begin{aligned}\langle\phi_p|\mathbf{I}_A\cdot\mathbf{I}_B|\phi_q\rangle = &\sum_{I_{AB}=|I_A-I_B|}^{|I_A+I_B|} \left(I_{AB}+\frac{1}{2}\right) \\ &\times \sqrt{(2F_A+1)(2F_A'+1)} \\ &\times \begin{Bmatrix} I_A & I_B & I_{AB} \\ F & S & F_A \end{Bmatrix}\begin{Bmatrix} I_A & I_B & I_{AB} \\ F & S & F_A' \end{Bmatrix} \\ &\times [I_{AB}(I_{AB}+1) - I_A(I_A+1) - I_B(I_B+1)], \end{aligned} \tag{A4}$$

where

$$\mathbf{I}_{AB} = \mathbf{I}_A + \mathbf{I}_B.$$

Using Eqs. (A3) and (A4) to evaluate the matrix elements $\langle\phi_p|H_1|\phi_q\rangle$ appearing in Eq. (A2) yields analytic expressions for the second-order energy corrections, and simplification of these expressions yields the formulas given in Tables I and II.

Since the subspaces Y can be labeled with the quantum numbers I_A, I_B, and F, second-order shifts are due to couplings between states that have the same values of these quantum numbers but distinct zero-order energies. When the values of I_A, I_B, and F uniquely specify $E^{(0)}$, the second-order shift is zero for the corresponding energy level, as illustrated in Tables I and II.

[1] D. I. Hoult and R. E. Richards, J. Magn. Reson. **24**, 71 (1976).
[2] J. Cavanagh, W. J. Fairbrother, A. G. Palmer III, M. Rance, and N. J. Skelton, *Protein NMR Spectroscopy: Principles and Practice* (Academic Press, Amsterdam, 2007).
[3] M. Hunter, in *Annual Reports on NMR Spectroscopy*, edited by G. A. Webb (Academic Press, 2012), Vol. 76, pp. 139–164; A. Mohorič and J. Stepišnik, Prog. NMR Spectrosc. **54**, 166 (2009).
[4] S. Xu, C. W. Crawford, S. Rochester, V. Yashchuk, D. Budker, and A. Pines, Phys. Rev. A **78**, 013404 (2008).
[5] P. T. Callaghan, A. Coy, R. Dykstra, C. D. Eccles, M. E. Halse, M. W. Hunter, O. R. Mercier, and J. N. Robinson, Appl. Magn. Reson. **32**, 63 (2007).
[6] S. Appelt, H. Kühn, F. W. Häsing, and B. Blümich, Nat. Phys. **2**, 105 (2006).
[7] M. E. Halse, A. Coy, R. Dykstra, C. Eccles, M. Hunter, R. Ward, and P. T. Callaghan, J. Magn. Reson. **182**, 75 (2006).
[8] A. Mohorič, G. Planinšič, M. Kos, A. Duh, and J. Stepišnik, Instrum. Sci. Technol. **32**, 655 (2004).
[9] M. P. Ledbetter, T. Theis, J. W. Blanchard, H. Ring, P. Ganssle, S. Appelt, B. Blümich, A. Pines, and D. Budker, Phys. Rev. Lett. **107**, 107601 (2011).
[10] L. Trahms and M. Burghoff, Magn. Reson. Imaging **28**, 1244 (2010).
[11] V. S. Zotev, A. N. Matlashov, P. L. Volegov, I. M. Savukov, M. A. Espy, J. C. Mosher, J. J. Gomez, and R. H. Kraus, Jr., J. Magn. Reson. **194**, 115 (2008).
[12] J. Bernarding, G. Buntkowsky, S. Macholl, S. Hartwig, M. Burghoff, and L. Trahms, J. Am. Chem. Soc. **128**, 714 (2006); M. Burghoff, S. Hartwig, L. Trahms, and J. Bernarding, Appl. Phys. Lett. **87**, 054103 (2005).
[13] R. McDermott, S. Lee, B. ten Haken, A. H. Trabesinger, A. Pines, and J. Clarke, Proc. Natl. Acad. Sci. U.S.A. **101**, 7857 (2004).
[14] A. H. Trabesinger, R. McDermott, S. Lee, M. Mck, J. Clarke, and A. Pines, J. Phys. Chem. A **108**, 957 (2004); R. McDermott, A. H. Trabesinger, M. Mck, E. L. Hahn, A. Pines, and J. Clarke, Science **295**, 2247 (2002).
[15] J. W. Blanchard, M. P. Ledbetter, T. Theis, M. C. Butler, D. Budker, and A. Pines, J. Am. Chem. Soc. **135**, 3607 (2013).
[16] T. Theis, M. P. Ledbetter, G. Kervern, J. W. Blanchard, P. J. Ganssle, M. C. Butler, H. D. Shin, D. Budker, and A. Pines, J. Am. Chem. Soc. **134**, 3987 (2012).
[17] T. Theis, P. Ganssle, G. Kervern, S. Knappe, J. Kitching, M. P. Ledbetter, D. Budker, and A. Pines, Nat. Phys. **7**, 571 (2011).
[18] M. Ledbetter, C. Crawford, A. Pines, D. Wemmer, S. Knappe, J. Kitching, and D. Budker, J. Magn. Reson. **199**, 25 (2009).
[19] D. B. Zax, A. Bielecki, K. W. Zilm, A. Pines, and D. P. Weitekamp, J. Chem. Phys. **83**, 4877 (1985).
[20] D. Zax, A. Bielecki, K. Zilm, and A. Pines, Chem. Phys. Lett. **106**, 550 (1984).
[21] D. P. Weitekamp, A. Bielecki, D. Zax, K. Zilm, and A. Pines, Phys. Rev. Lett. **50**, 1807 (1983).
[22] M. Packard and R. Varian, Phys. Rev. **93**, 941 (1954).
[23] V. S. Zotev, T. Owens, A. N. Matlashov, I. M. Savukov, J. J. Gomez, and M. A. Espy, J. Magn. Reson. **207**, 78 (2010).
[24] M. E. Halse and P. T. Callaghan, J. Magn. Reson. **195**, 162 (2008).
[25] M. C. Butler, G. Kervern, T. Theis, M. P. Ledbetter, P. J. Ganssle, J. W. Blanchard, D. Budker, and A. Pines, "Parahydrogen-induced polarization at zero magnetic field," J. Chem. Phys. (to be published).
[26] B. C. Hamans, A. Andreychenko, A. Heerschap, S. S. Wijmenga, and M. Tessari, J. Magn. Reson. **212**, 224 (2011).
[27] S. Appelt, F. W. Häsing, H. Kühn, J. Perlo, and B. Blümich, Phys. Rev. Lett. **94**, 197602 (2005).
[28] Y. S. Greenberg, Rev. Mod. Phys. **70**, 175 (1998).
[29] D. Yu, N. Garcia, and S. Xu, Concepts Magn. Reson. **34A**, 124 (2009).
[30] D. Budker and M. Romalis, Nat. Phys. **3**, 227 (2007).
[31] I. M. Savukov and M. V. Romalis, Phys. Rev. Lett. **94**, 123001 (2005).
[32] V. Shah, S. Knappe, P. D. D. Schwindt, and J. Kitching, Nat. Photon. **1**, 649 (2007).
[33] M. Espy, M. Flynn, J. Gomez, C. Hanson, R. Kraus, P. Magnelind, K. Maskaly, A. Matlashov, S. Newman, T. Owens, M. Peters, H. Sandin, I. Savukov, L. Schultz, A. Urbaitis, P. Volegov, and V. Zotev, Supercond. Sci. Technol. **23**, 034023 (2010).
[34] S. K. Lee, M. Mößle, W. Myers, N. Kelso, A. H. Trabesinger, A. Pines, and J. Clarke, Magn. Reson. Med. **53**, 9 (2005).
[35] G. Planinšič, J. Stepišink, and M. Kos, J. Magn. Reson. A **110**, 170 (1994).
[36] S. Xu, E. Harel, D. J. Michalak, C. W. Crawford, D. Budker, and A. Pines, J. Magn. Reson. Imaging **28**, 1299 (2008).
[37] M. Mößle, S.-I. Han, W. R. Myers, S.-K. Lee, N. Kelso, M. Hatridge, A. Pines, and J. Clarke, J. Magn. Reson. **179**, 146 (2006).
[38] A. N. Matlachov, P. L. Volegov, M. A. Espy, J. S. George, and R. H. Kraus, Jr., J. Magn. Reson. **170**, 1 (2004).
[39] O. R. Mercier, M. Hunter, and P. Callaghan, Cold Regions Sci. Technol. **42**, 96 (2005).
[40] A. Legchenko, J.-M. Baltassat, A. Beauce, and J. Bernard, J. Appl. Geophys. **50**, 21 (2002).
[41] J. N. Robinson, A. Coy, R. Dykstra, C. D. Eccles, M. W. Hunter, and P. T. Callaghan, J. Magn. Reson. **182**, 343 (2006).
[42] S. Appelt, F. W. Häsing, H. Kühn, and B. Blümich, Phys. Rev. A **76**, 023420 (2007); S. Appelt, F. W. Häsing, H. Kühn, U. Sieling, and B. Blümich, Chem. Phys. Lett. **440**, 308 (2007).
[43] S. Appelt, F. W. Häsing, U. Sieling, A. Gordji-Nejad, S. Glöggler, and B. Blümich, Phys. Rev. A **81**, 023420 (2010).
[44] M. E. Halse, P. T. Callaghan, B. C. Feland, and R. E. Wasylishen, J. Magn. Reson. **200**, 88 (2009).
[45] T. Theis, J. W. Blanchard, M. C. Butler, M. P. Ledbetter, D. Budker, and A. Pines, "Chemical analysis using J-coupling multiplets in zero-field NMR," (unpublished).
[46] C. Cohen-Tannoudji, B. Diu, and F. Laloë, *Quantum Mechanics* (Wiley, New York, 1977), pp. 1072–1085.
[47] M. Auzinsh, D. Budker, and S. Rochester, *Optically Polarized Atoms: Understanding Light-Atom Interactions* (Oxford, New York, 2010).
[48] C. Cohen-Tannoudji, B. Diu, and F. Laloë, *Quantum Mechanics* (Wiley, New York, 1977), pp. 1048–1058.
[49] See pp. 46–49 of Ref. 47.